





Article

Archaeal Lipids Regulating the Trimeric Structure Dynamics of Bacteriorhodopsin for Efficient Proton Release and Uptake

Sijin Chen ^{1,†}, Xiaoyan Ding ^{1,2,†}, Chao Sun ¹, Fei Wang ¹, Xiao He ^{3,4,*} , Anthony Watts ^{2,*} and Xin Zhao ^{1,*} 

¹ Department of Physics, School of Physics and Electronic Science, East China Normal University, 500 Dongchuan Road, Minhang District, Shanghai 200241, China; 52194700015@stu.ecnu.edu.cn (S.C.); xiaoyan.ding@bioch.ox.ac.uk (X.D.); csun@phy.ecnu.edu.cn (C.S.); 51194700053@stu.ecnu.edu.cn (F.W.)

² Department of Biochemistry, University of Oxford, South Park Road, Oxford OX1 3QU, UK

³ Shanghai Engineering Research Center of Molecular Therapeutics and New Drug Development, Shanghai Frontiers Science Center of Molecule Intelligent Syntheses, School of Chemistry and Molecular Engineering, East China Normal University, Shanghai 200062, China

⁴ School of Chemistry and Molecular Engineering, NYU-ECNU Center for Computational Chemistry at NYU Shanghai, East China Normal University, Shanghai 200062, China

* Correspondence: xiaohe@phy.ecnu.edu.cn (X.H.); anthony.watts@bioch.ox.ac.uk (A.W.); xzhao@phy.ecnu.edu.cn (X.Z.)

† These authors contributed equally to this work.

Abstract: S-TGA-1 and PGP-Me are native archaeal lipids associated with the bacteriorhodopsin (bR) trimer and contribute to protein stabilization and native dynamics for proton transfer. However, little is known about the underlying molecular mechanism of how these lipids regulate bR trimerization and efficient photocycling. Here, we explored the specific binding of S-TGA-1 and PGP-Me with the bR trimer and elucidated how specific interactions modulate the bR trimeric structure and proton release and uptake using long-term atomistic molecular dynamic simulations. Our results showed that S-TGA-1 and PGP-Me are essential for stabilizing the bR trimer and maintaining the coherent conformational dynamics necessary for proton transfer. The specific binding of S-TGA-1 with W80 and K129 regulates proton release on the extracellular surface by forming a “Glu-shared” model. The interaction of PGP-Me with K40 ensures proton uptake by accommodating the conformation of the helices to recruit enough water molecules on the cytoplasmic side. The present study results could fill in the theoretical gaps of studies on the functional role of archaeal lipids and could provide a reference for other membrane proteins containing similar archaeal lipids.

Keywords: bacteriorhodopsin; archaeal lipids; S-TGA-1 and PGP-Me; lipid–protein interactions; trimer stability; proton release and uptake



Citation: Chen, S.; Ding, X.; Sun, C.; Wang, F.; He, X.; Watts, A.; Zhao, X. Archaeal Lipids Regulating the Trimeric Structure Dynamics of Bacteriorhodopsin for Efficient Proton Release and Uptake. *Int. J. Mol. Sci.* **2022**, *23*, 6913. <https://doi.org/10.3390/ijms23136913>

Academic Editor: Małgorzata Borówko

Received: 19 May 2022

Accepted: 20 June 2022

Published: 21 June 2022

Publisher's Note: MDPI stays neutral with regard to jurisdictional claims in published maps and institutional affiliations.



Copyright: © 2022 by the authors. Licensee MDPI, Basel, Switzerland. This article is an open access article distributed under the terms and conditions of the Creative Commons Attribution (CC BY) license (<https://creativecommons.org/licenses/by/4.0/>).

1. Introduction

Biomembranes consist of lipids, proteins, and carbohydrates and are fundamental to life. They are responsible for the cell envelopes that enable cells to absorb nutrients and exclude the most harmful agents from entering cells. They are also very dynamic in terms of structure, enabling interactions among proteins and between proteins and lipids to provide temporal associations that are significant to membrane functions [1]. The basic unit of a membrane is a bilayer that is formed by phospholipids and sphingolipids that are organized into two layers with their polar headgroups along the two surfaces and their acyl chains creating a nonpolar domain in between.

Transmembrane proteins are embedded in the lipid bilayer and play a crucial role in biological processes such as ion transport, signal transduction, and communication, making ideal drug targets [1,2]. Phospholipids are indispensable to transmembrane proteins, and increasing evidence indicates that the functions of transmembrane proteins are affected by different lipid environments [3–8] and specific lipid–protein interactions [9–15]. However, only a few high-resolution crystallographic data describing the details of protein–lipid

interactions in transmembrane proteins are available. For example, the lipid polar head-groups in the K^+ channel protein Kv2.1 [16] and light-adapted bacteriorhodopsin (bR) have not yet been well resolved [17,18]. In addition, not many quantitative methods are available to identify specific lipid–protein interactions.

bR is a typical seven-transmembrane (7TM) light-driven proton pump found in the *Halobacterium halobium* (*H. halobium*) [19] and has served as an ideal model for studying the ion transport and energy conduction in membrane proteins for many years [20–24]. The retinal chromophore is covalently bound to a lysine residue on helix G and forms a protonated Schiff base (SB) linkage. The photoisomerization of all-trans retinal to the 13-cis isomer triggers conformation changes in the receptor to release a proton to the extracellular surface and uptake another one from the cytoplasmic bulk through a series of photo-intermediate states, including the intermediate states of K, L, M₁, M₂, M₂', N, and O [24–27]. A detailed description of the bR photocycle and the proton transfer steps is shown in Supplementary Materials Figure S1.

The bR purple membrane (PM) consists of approximately 90% polar lipids: 60% phospholipids and 30% glycolipids; the remaining 10% are mainly neutral squalene lipids [28–31]. Phospholipids are primarily made of phosphatidylglycerol (PG), phosphatidylglycerol sulfate (PGS), and phosphatidylglycerol phosphate methyl ester (PGP-Me). Glycolipids are mainly composed of archaeal glycardiolipin (GlyC), cardiolipin (bisphosphatidylglycerol, BPG), and glycolipid sulfate (3-HSO₃-Galp-β1,6-Manp-α1,2-Glcp-α1,1-sn-2,3-diphytanylglycerol, S-TGA-1). S-TGA-1 is a specific lipid located in the center of the bR trimer closure and is essential for intra-trimer stabilization [32–35]. PGP-Me is a particular lipid existing in the space of the adjacent bR monomers and acts as a glue to bridge contact between the bR monomers and maintain trimer stabilization [34–38] (Figure 1). Previous studies have revealed that these two polar lipids are essential to bR trimerization and proton transfer through specific interactions [17,32–35,37–55]. However, the detailed coupling mechanism of these specific lipids with the bR proton pumping function during proton release and uptake remains unclear due to the lipids being inaccessible commercially or for laboratory synthesis.

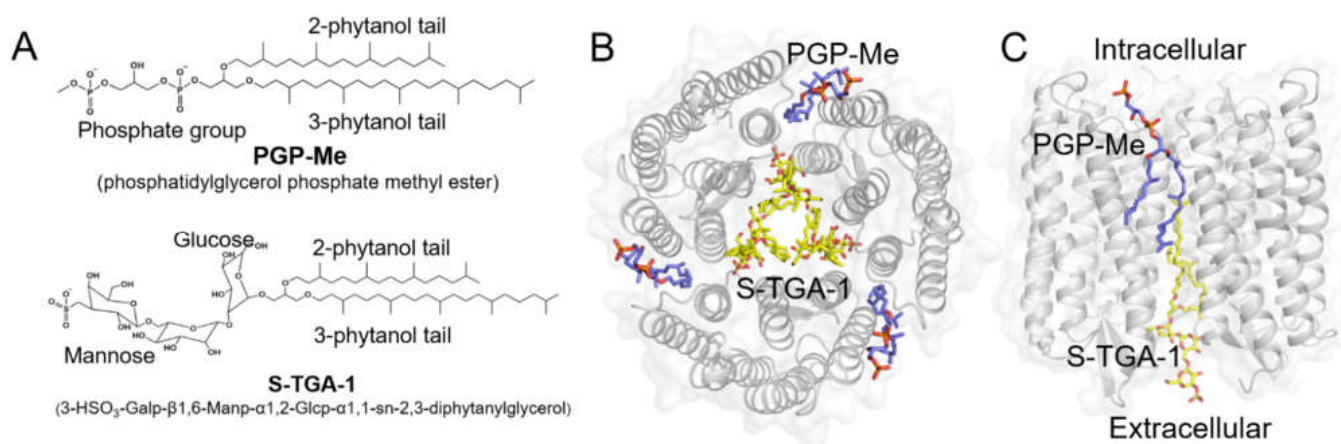


Figure 1. Schematic diagram of the structures of S-TGA-1, PGP-Me, and the bacteriorhodopsin (bR) trimer. (A) Molecular structures of S-TGA-1 and PGP-Me; (B,C) top and front view for the locations of S-TGA-1 (yellow sticks) and PGP-Me (dark blue sticks) within the bR trimer (grey cartoon).

On the other hand, molecular dynamic (MD) simulations are an ideal tool for bridging the gap by exploring specific lipid–protein interactions [56–63]. However, simulations in the early years were often confined to a single or a few mixed lipids [14,64,65], and the simulation time was not long enough (1–100 ns) [57,59,66]. In this paper, we carry out a long-term all-atom MD simulation (1 μ s) with the single-point mutagenesis to delineate the molecular mechanism of the specific interaction of S-TGA-1 and PGP-Me with bR during the proton release and uptake processes. Amber18 [67] and Gaussian16 [68] are

used to construct the S-TGA-1 and PGP-Me force fields, which are then embedded into the corresponding position of the protein via the PyMOL [69] and PPM web servers [70]. Our results provide an improved understanding of how archaeal lipids influence the bR trimeric structure and proton pumping function and provide inspiration for studying lipid–protein interactions in other membrane proteins, including these archaeal lipids. Supplementary Materials Table S1 summarizes the 10 simulation models used.

2. Results and Discussion

The dynamic functions of any membrane protein directly correspond to the conformational dynamics in the native membrane environment. Many studies have reported that the photocycle kinetics of bR are different in the native membrane and in the membrane mimics [18,38,44,51,52]. S-TGA-1 and PGP-Me are the specific archaeal lipids of PM, playing an important role in this difference by binding the bR. However, their interactions with the bR trimer have not been well resolved by X-ray crystallography [18], and so far, no long-term MD simulations (microsecond time scale) are available to gain insight into the dynamic binding of S-TGA-1 and PGP-Me with the bR trimer. Here, we sought to determine the specific interactions of S-TGA-1 and PGP-Me with the bR trimer through all-atom MD simulations over a length of 1 μ s.

2.1. Maintaining the Overall Coherent Dynamics by S-TGA-1 and PGP-Me Binding

The bR trimer achieved a smaller root mean square deviation (RMSD) with the lipids of POPC, S-TGA-1, and PGP-Me (denoted here as M1) than it did with only POPC lipids (M2) throughout the simulations (Figure 2A). The overall root mean square fluctuation (RMSF) of M1 was also less than M2 (Figure 2D and Table S2). All of the results indicate that S-TGA-1 and PGP-Me are conducive to bR trimer stabilization with appropriate dynamics. Previous research also mentioned the importance of S-TGA-1 and PGP-Me for the bR 2D crystal alignment and trimeric stabilization [34,36,42,44,52]. The effects of these two archaeal lipids on the dynamics of the bR trimer were then further examined separately by the membranes containing only the bR trimer, POPC, and S-TGA-1 (M3) or the bR trimer, POPC, and PGP-Me (M4). Our results showed that both S-TGA-1 and PGP-Me could stabilize the trimer's dynamic conformation, with S-TGA-1 being more prominent (Figure 2B,C,E,F), a finding that was consistent with the previous results [52]. In addition, the simulations showed that S-TGA-1 contributes to the order of the B-C loop, D-E loop, F-G loop, and helix D; PGP-Me promotes the order of the C-D loop, E-F loop, and helix E (Figure 2E,F and Table S2). As such, we suggest that S-TGA-1 and PGP-Me enhance the bR trimer's stability by mediating the dynamics of the extracellular and cytoplasmic sides, respectively. Several studies have confirmed that S-TGA-1 and PGP-Me are essential for the bR's array structure and stabilization [34,36,44,52].

A more uniform and coherent correlation in M1, but an incoherent and localized correlation in M2, was observed by the dynamic cross-correlation map (DCCM) and dynamic cross-correlation network (DCCN) analyses [71–74] (Figure 2G,J,K). The differences observed in M2 were also identified in M3 and M4; although the overall correlation was not as pronounced as in M1 (Figure 2H,I,L,M). Repeated simulations also observed similar results, as shown in Figure S2. These results indicate that S-TGA-1 and PGP-Me are conducive to stabilizing the bR trimer and have more consistent dynamics for different functional domains. Previous studies have also suggested that archaeal lipids are needed for the adjoining monomers to interact and form a trimer [38,41]. The absence of S-TGA-1 disturbed the dynamic correlation of Helix D and the cytoplasmic region (E-F loop), and the lack of PGP-Me affected the dynamic correlation of the extracellular region of Helix D, indicating that the regulation of the bR dynamic conformation by S-TGA-1 and PGP-Me was synergistic instead of independent. These observations suggested that S-TGA-1 and PGP-Me can maintain the appropriate dynamics to ensure the bR trimer has enough coherent flexibility for proton release and uptake on both sides of the surfaces [18,38,44,51,52].

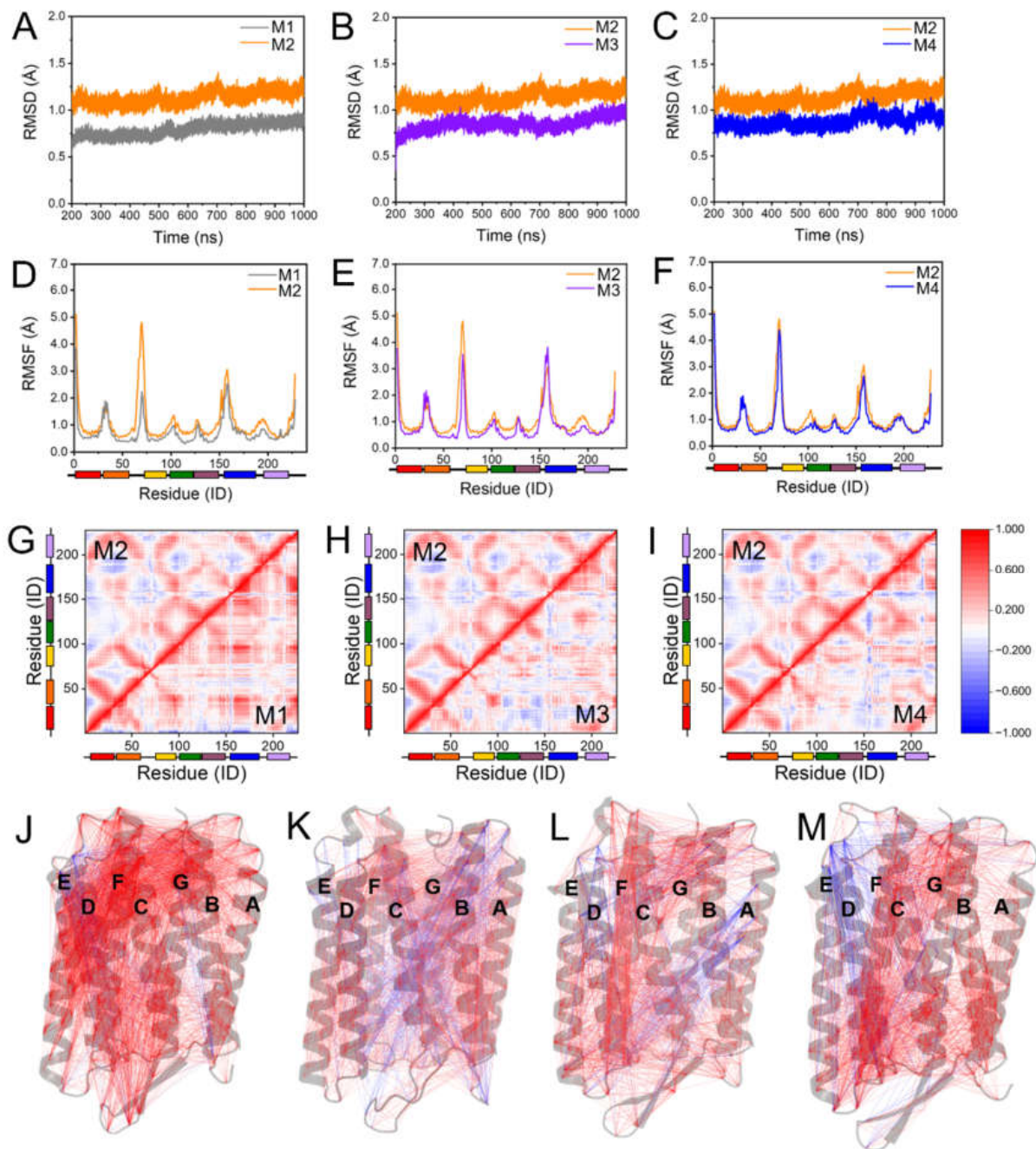


Figure 2. The influence of S-TGA-1 and PGP-Me on the dynamic stability of the bR trimer. (A–C) Time evolutions of the root mean square deviation (RMSD) of the C α atoms during the simulations. (A) M1 (bR trimer with POPC, S-TGA-1, and PGP-Me, grey line) vs. M2 (bR trimer with POPC only, orange line); (B) M3 (bR trimer with POPC and S-TGA-1, purple line) vs. M2; (C) M4 (bR trimer with POPC and PGP-Me, blue line) vs. M2; (D–F) time evolutions of root mean square fluctuations (RMSF) of the C α atoms: (D) M1 vs. M2; (E) M3 vs. M2; (F) M4 vs. M2; (G–I) dynamic cross-correlated map (DCCM) analyses of the C α atoms; (G) M1 vs. M2; (H) M3 vs. M2; (I) M4 vs. M2. The upper left triangle represents M1. The color scale represents the correlation intensity from the maximum negative value (−1) to the ultimate positive value (+1); (J–M) dynamic cross-correlation network (DCCN) analyses of residue–residue cross-correlations from M1 to M4. The grey cartoon represents the bR structure of Monomer1 (one of the three monomers in the bR trimer), and blue and red lines indicate the negatively and positively correlated motions, respectively.

The headgroup of S-TGA-1 interacted with Y64, L66, T67, W80, and K129 through hydrogen bond (H-bond) interactions; the indole ring of W80 was almost parallel to the trimer axis due to its Pi-alkyl hydrophobic interaction with the 2-phytanol tail of S-TGA-1; G113, G116, and G120 formed a groove to accommodate the 3-phytanol tail through hydrophobic interactions on the extracellular side (Figure 3A,B). The lifetime of these H-bonds indicated that the contact remained intact throughout all of the simulations, with the exception of a slightly weaker H-bond between T67 and the 3-hydroxy of mannose (Figure 3C). K129 may form a salt bridge with the galactosyl-3-sulfate group of S-TGA-1 (Figure 3D). Some of the above interactions were also mentioned in earlier crystal structure studies [17,32,75]. In addition, we identified extra hydrophobic interactions involving V69, P70, A84, L87, F88, and V124 that have not been previously reported in any crystal structures (Figure 3A). On the cytoplasmic side, the PGP-Me headgroup had H-bond interactions with K40, G155, and T157 (Figure 4A,B), with a lifetime of about 1 μ s for G155 and T157 and a lifetime longer than 700 ns for K40 (Figure 4C); and the ϵ -amino group of K40 may come into contact with the polar headgroup of PGP-Me via a salt bridge (Figure 4D). In addition, several residues on the cytoplasmic side of helices B, D, and E (L28, M32, Y43, A44, T47, A51, A110, A114, I117, I140, A143, A144, Y147, and Y150) had hydrophobic contact with both of the phytanol tails of PGP-Me (Figure 4A). These specific lipid-protein interactions provide connections between the adjacent monomers on both ends of the bR trimer to maintain the global conformational dynamic stability of the whole protein complex for proton release and uptake via coherent correlations.

2.2. Coupling of S-TGA-1 with the Extracellular Surface of bR for Proton Release

Previous studies have reported that S-TGA-1 and PGP-Me are essential for bR to carry out its normal photocycle and proton pumping activity [38,39,42,44,49,51–53]. The results above also indicated that the archaeal lipids could regulate the stability and dynamic conformation of the bR trimer. However, it remains unclear how S-TGA-1 and PGP-Me interact with the bR trimer to regulate its function-related dynamic conformation. Here, we further explored how specific lipid-protein interactions influence bR proton release and uptake according to a series of simulations on different mutants.

Further analysis of M1 revealed that the interactions between E194 and E204, the two crucial residues for proton release, were perturbed by S-TGA-1. In the presence of S-TGA-1, our simulations showed that E194 and E204 are close enough to form a “Glu-shared” model to cast the proton between them for effective proton release (Figure 5A,B and Table S3), as reported previously [76–80]. Previous studies showed that A51 is stationary during simulations [81], so the distance from A51 to R82 can be used to monitor R82 movement during the photocycle. It is clear that R82 couples with the retinal binding pocket in dark-adapted bR and affects the proton release complex (PRC) for proton release in the M state [75]. Thus, we may be able to indirectly investigate the influence of S-TGA-1 on E194 and E204 through the distance changes from Y83 to E194 and from A51 to R82. Interestingly, the distances from Y83 to E194 and from A51 to R82 were not much different in M1 and M2 (Figure 5C,D and Table S3), but there were apparent displacements of both W80 and Y83 on helix C towards E204 (Figure 5A), implying that the displacements of W80 and Y83 have an impact on E194...E204 packing. Such shifts may originate from W80's pi-alkyl hydrophobic interaction with S-TGA-1. In addition, R134 has H-bond interactions with T128 on the D-E loop, E194 on the F-G loop, and K129 on the D-E loop to produce cascade perturbations on the F-G loop [75,82]. Therefore, it is worth considering whether the interaction of K129 with S-TGA-1 also affects the “Glu-shared” model. To elucidate the underlying molecular mechanism of how W80...S-TGA-1 and K129...S-TGA-1 specific interactions regulate the proton release, we constructed simulations on W80A (M5, the membrane containing the W80A-bR trimer, POPC, S-TGA-1, and PGP-Me lipids) and K129L (M6, the membrane containing the K129L-bR trimer, POPC, S-TGA-1, and PGP-Me lipids) mutations.

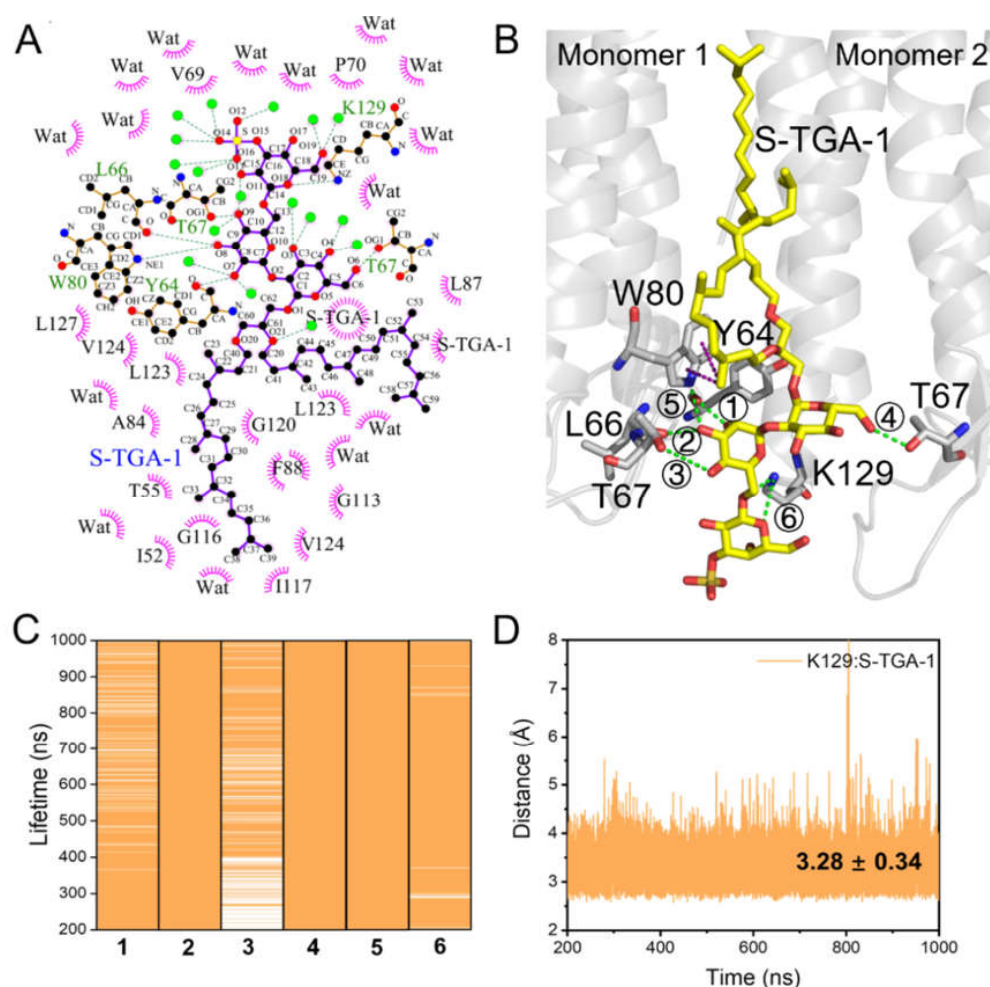


Figure 3. Schematic representation of S-TGA-1 binding to the bR trimer. (A) The LigPlot+ diagrams of the S-TGA-1 binding sites from the last snapshot of M1; the green dotted lines and the pink spoked arcs represent hydrogen bond (H-bond) and hydrophobic interactions, respectively; (B) the possible H-bond (green dotted line) and Pi-alkyl hydrophobic interactions (purple dotted line) between S-TGA-1 with bR. Monomer1 and Monomer2 represent the two adjacent monomers in the bR trimer. The grey sticks represent the interacting residues, and the yellow sticks represent S-TGA-1; (C) evaluation of the lifetimes of the H-bond interactions for S-TGA-1; see (B) for the description of the numbers: (1) Y64...2-hydroxyl of mannose; (2) L66...2-hydroxyl of mannose; (3) T67...3-hydroxyl of mannose; (4) T67...6-hydroxyl of glucose; (5) W80...2-hydroxyl of mannose; (6) K129...ether group of galactosyl-3-sulfate; (D) time evolution of the distance between K129 and the galactosyl-3-sulfate of S-TGA-1. These interaction modes were reproducible in the second time-repeating simulation, as shown in Figures S3 and S4.

The RMSDs of M5 and M6 over the total simulation were more significant than that of M1, and the same for RMSFs of the C-D loop, helices F and G, with the difference caused by W80A more prominent (Figure 6A–D). These results indicate that W80 and K129 could mediate the connection between the adjacent monomeric helices by binding with S-TGA-1 to maintain appropriate dynamics for the bR trimer. DCCM and DCCN analyses showed that the change in inter-residue interactions caused the negative correlations to increase significantly, especially on the extracellular surface (Figure 6E–H), resulting in reduced stability for the bR trimer.

We further monitored the detailed changes of several key residues and water molecules on the extracellular side caused by the W80A and K129L mutations. For the membrane of the W80A-bR trimer with S-TGA-1 and PGP-Me (M5), E194–E204's "Glu-shared" pattern was not observed (Figure 7A and Table S4), Y83 still formed an H-bond with E194, and R82's

guanidine group demonstrated little change (Figure 7B,C and Table S4). However, Y83 underwent a significant displacement, moving to a position similar to what we observed in M2 (Figure 7D,E), indicating that the hydrophobic interactions between W80 and S-TGA-1 may regulate Y83 conformation to encourage E194 to be closer to E204. The H-bond between E194 and E204 fluctuated in M7 (membrane of the W80A-bR trimer without S-TGA-1 and PGP-Me), and the Y83 and R82 displacements were also significantly different from what we observed in M5 (Figures S6 and S7, Table S4). All further evidence suggested that the Pi-Alkyl hydrophobic interaction between W80 and S-TGA-1 promotes the formation of the “Glu-shared” model favorable for proton release through regulating Y83. Weik et al. have proposed that the interactions between aromatic residues, especially tryptophan, and lipids are essential for bR’s proton pumping function [49]. Our present simulation results more concretely illustrate this proposal.

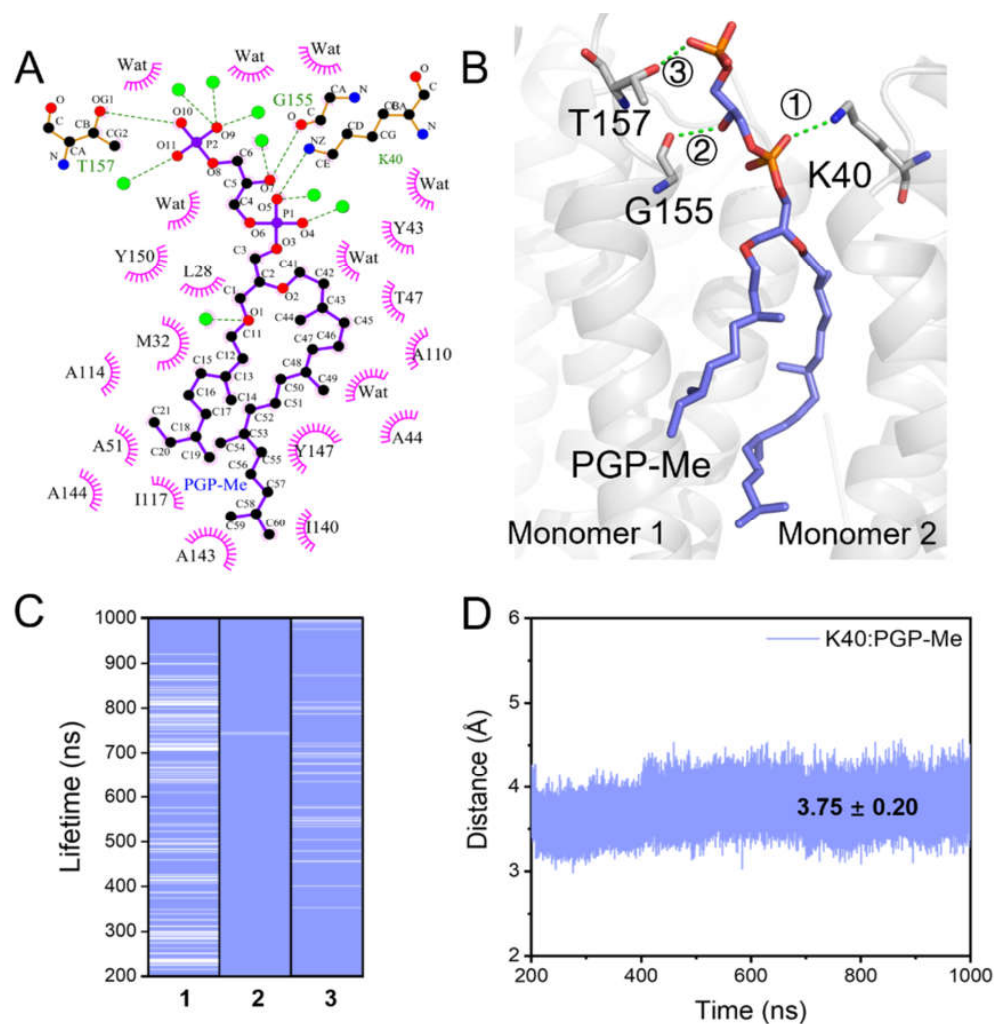


Figure 4. Schematic representation of PGP-Me binding to the bR trimer. (A) The LigPlot+ diagrams of the PGP-Me binding sites from the last snapshot of M1; the green dotted lines and the pink spoked arcs represent H-bond and hydrophobic interactions, respectively; (B) the possible H-bond interactions (green dotted line) between PGP-Me and the two adjacent monomers in the bR trimer. The grey sticks represent the residues interacting with PGP-Me via H-bond, and the dark-blue sticks represent PGP-Me; (C) evaluation of the lifetimes of the H-bond interactions for PGP-Me; see (B) for the description of the numbers: (1) K40...O5 of the phosphate group; (2) G155...O7 of the phosphate group; (3) T157...O10 of the phosphate group; (D) the evolution of the distance between K129 and the galactosyl-3-sulfate of S-TGA-1. These interaction modes were reproducible in the second time-repeating simulation, as shown in Figures S3 and S4.

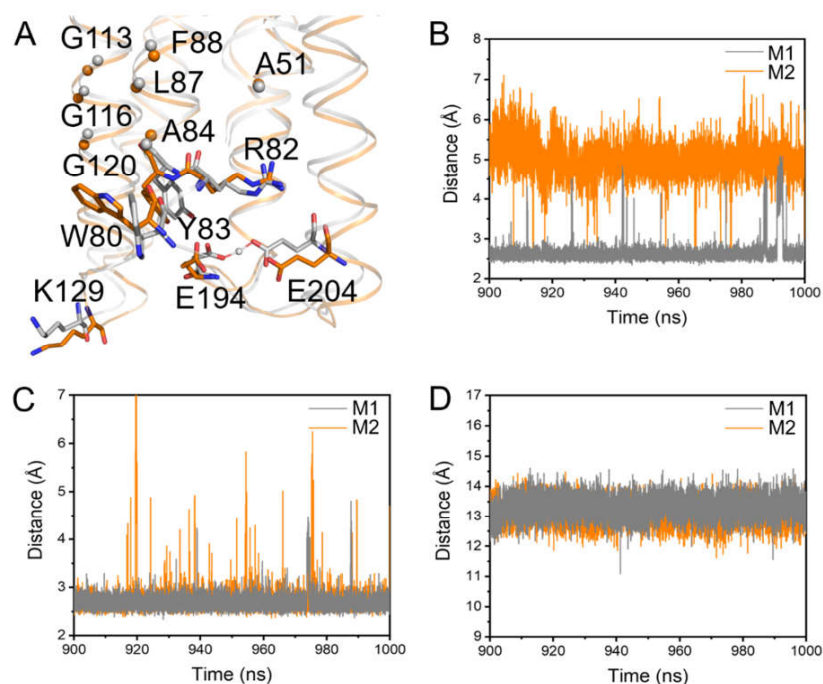


Figure 5. Conformation changes on the extracellular side induced by S-TGA-1. (A) Detailed changes in the key residues in the extracellular side in M1 (grey cartoon, sticks, and spheres) relative to M2 (orange cartoon, sticks, and spheres); (B–D) the evolution of the distance between the key residues from the last 100 ns simulations of M1 (grey line) and M2 (orange line): (B) E194–E204; (C) Y83–E194; (D) R82–A51. Repeated simulations could reproduce these behaviors (Figure S5 and Table S3).

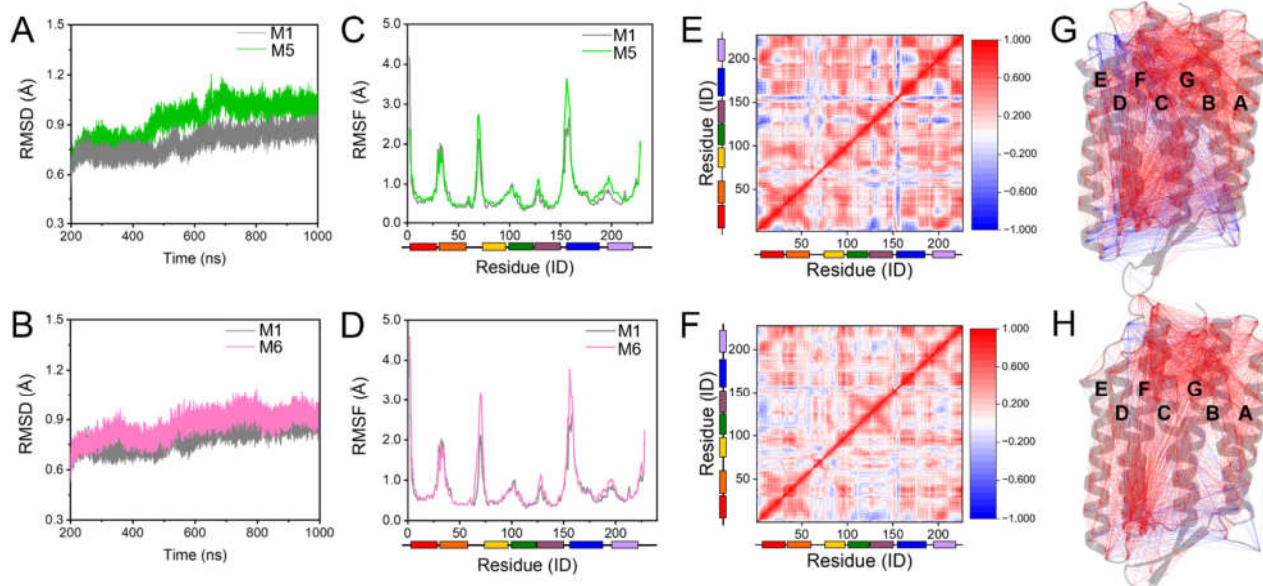


Figure 6. The influence of the W80...S-TGA-1 and K129...S-TGA-1 interactions on the dynamic stability of the bR trimer. (A,B) Time evolutions of the RMSD of the C α atoms during the simulations; (A) M1 (grey line) vs. M5 (membrane containing the W80A-bR trimer, POPC, S-TGA-1, and PGP-Me lipids, green line); (B) M1 vs. M6 (membrane containing the K129L-bR trimer, POPC, S-TGA-1, and PGP-Me lipids, pink line); (C,D) time evolutions of RMSF of the C α atoms: (C) M1 vs. M5; (D) M1 vs. M6; (E,F) DCCM analyses of the C α atoms for M5 and M6. The color scale represents the correlation intensity from the maximum negative value (−1) to the ultimate positive value (+1); (G,H) DCCN analyses of residue–residue cross-correlations for M5 and M6. The grey cartoon represents the bR structure of Monomer1, and blue and red lines indicate the negatively and positively correlated motions, respectively.

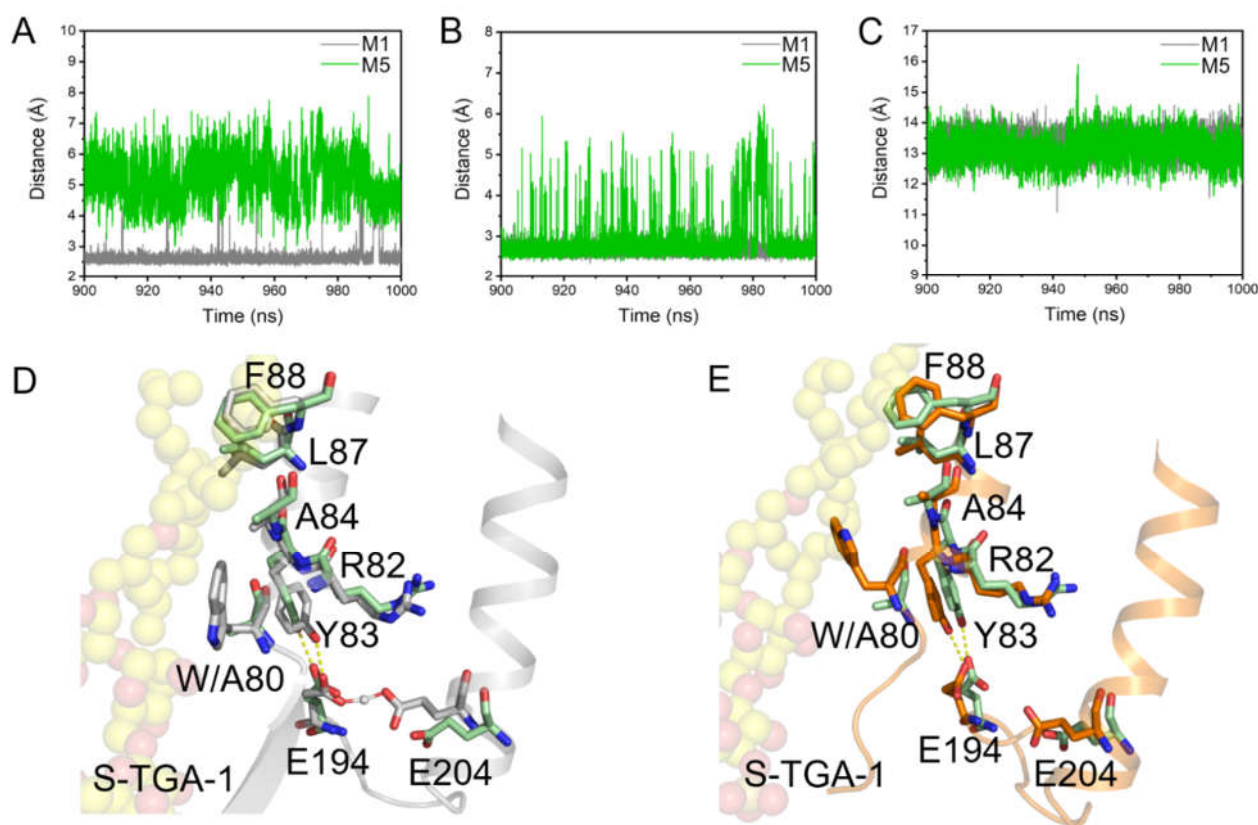


Figure 7. Dynamic conformation changes of the key residues on the extracellular side of bR induced by the W80A mutation. (A–C) The evolution of the distance between the key residues from the last 100 ns simulations of M1 (grey line) and M5 (green line): (A) E194–E204; (B) Y83–E194; (C) R82–A51. This behavior could be reproduced in the second time-repeat simulation (Figure S8 and Table S4); (D,E) superimposed drawing of several key residues on the extracellular side: (D) M1 (grey cartoon and sticks) vs. M5 (pale green sticks); (E) M2 (orange cartoon and sticks) vs. M5. Yellow spheres highlight S-TGA-1.

The H-bond interaction between E194 and E204 was also perturbed in the M7 of the K129L-bR trimer with the lipids of POPC, S-TGA-1, and PGP-Me (Figure 8A and Table S5); however, this perturbation was not observed in the M8 of the K129L-bR trimer without S-TGA-1 and PGP-Me (Figure S9A and Table S5), suggesting the changes of the “Glu-shared” model were due to the loss of contact between K129 and S-TGA-1. The H-bond between R134 and E194 was unstable (Figure 8B and Table S5), and there were more water molecules around K129 and T128 in M6 (Figure 8C), but this was not the case in M8 (Figures S9B,C, S10, and Table S5). Therefore, we proposed that the broken H-bond interaction between K129 and S-TGA-1 could attract more water molecules to gather around K129 and T128, causing increased fluctuations in the D-E loop. The F-G loop was perturbed through agitation in the H-bond chain of T128···R134···E194; thereby destabilizing the H-bond interaction between E194 and E204 (Figure 8D,E). The significantly increased fluctuation and incoherent correlations of the D-E and F-G loops agree further with our proposal.

It is well known that proton release occurs in the M state, and the rapid release is beneficial for accelerating the M state decay and improving the proton pumping efficiency [24,83,84]. Our simulations demonstrated that W80 and K129 significantly influence E194···E204 to form the “Glu-shared” model through interacting with S-TGA-1, which is conducive to promoting proton release during the short lifetime of the M state [49,52] (Figure S12).

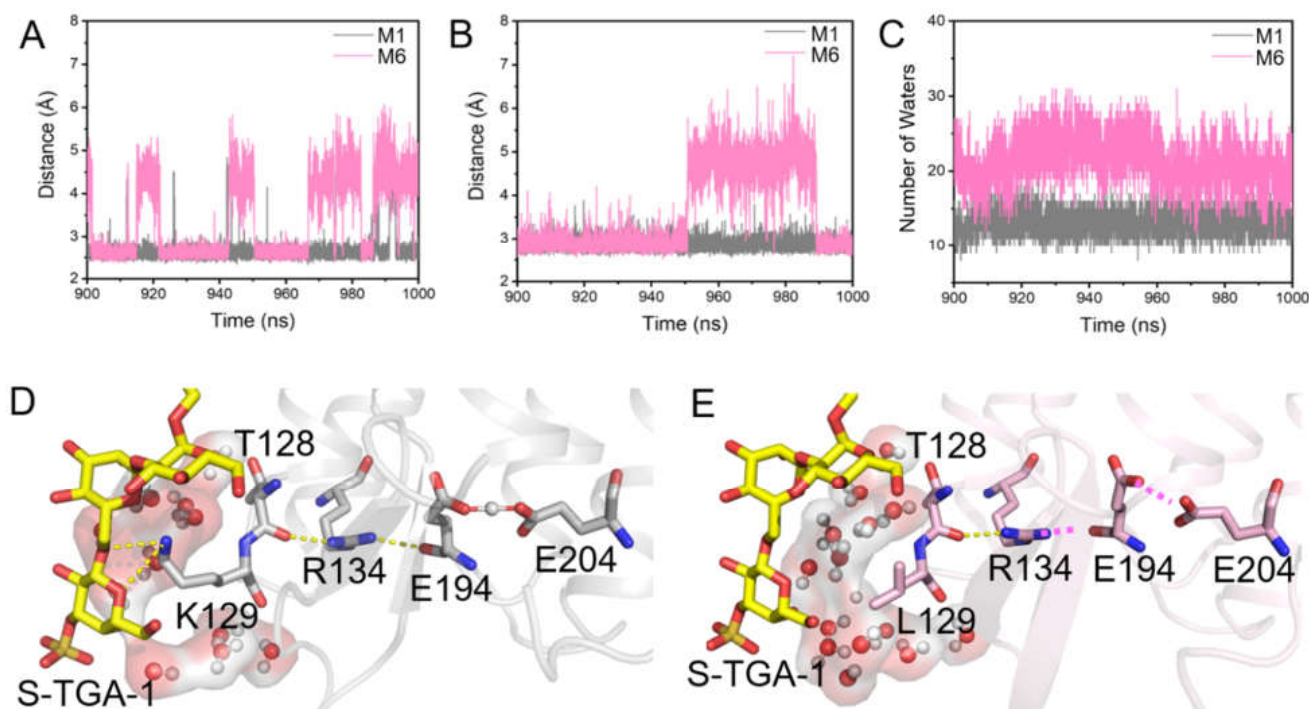


Figure 8. Dynamic conformational changes of the key residues on the extracellular side of bR induced by the K129L mutation. (A,B) The evolution of the distance between the key residues from the last 100 ns simulations of M1 (grey line) and M6 (pink line): (A) E194-E204; (B) R134-E194; (C) time series of the number of water molecules around K/L129 and T128 in the last 100 ns simulations of M1 (grey line) and M6 (pink line). This behavior could be reproduced in the second time-repeat simulation (Figure S11 and Table S5); (D,E) schematic diagrams of the H-bond network connecting K129 and the proton release complex (PRC) in M1 (D) and M6 (E). The grey cartoon and sticks were used for M1, pink cartoon and sticks were used for M6, yellow sticks represent S-TGA-1, red spheres, and the transparent surface indicates the water chains around K129 and T128, respectively. The pink dotted lines show unstable H-bond interactions.

2.3. Coupling of PGP-Me with the Cytoplasmic Surface of bR for Proton Uptake

Formation of the transient water chain and having an “open” conformation in the cytoplasmic half channel are essential for the proton uptake in the later stage of the bR photocycle [85,86]. Any changes in the opening and closing of the helix conformation and the number of water molecules induced by PGP-Me may affect the proton uptake. On the cytoplasmic side, the helices A, B, D, E, and the E-F loop in M1 were quite different from M2 according to our simulations (Figure 9A), but were consistent with the bR crystal structure containing PGP-Me (Figure S13) [32,35]. A further comparison found that PGP-Me resulted in a larger opening (Figures 9B and S14, and Table S6), and such conformational differences significantly impacted the number of water molecules in the accessible region of the cytoplasm. More water molecules aggregated around the hydrophobic residues on the cytoplasmic surface of M1 than M2 (Figure 9C,D).

Otomo et al. found that bR cannot self-assemble *in vivo* to form PM upon the mutation of K40 to a neutral residue, resulting in an impaired proton pumping function [87]. Therefore, we performed simulations on the K40L-bR trimer (M9, the membrane containing the K40L-bR trimer, POPC, S-TGA-1, and PGP-Me lipids) to explore how the K40...PGP-Me interaction affects the protein trimer stability and proton uptake. The RMSD of the K40L-bR trimer was slightly higher than that of M1, implying that the specific K40...PGP-Me interaction may contribute to stabilizing the bR trimer (Figure 10A). The number of water molecules on the cytoplasmic surface increased, with helix A moving away from its initial position and having a more flexible open conformation (Figure 10B,C and Table S6). However, a slight change was observed in the K40L mutant without S-TGA-1 and PGP-Me in

M10 (Figures S15 and S16, Table S6). Therefore, we speculate that the interaction between K40 and PGP-Me may cause changes in the helices and the number of water molecules at the cytoplasmic terminal. In the late M state of bR, the cytoplasmic side of helices E and F slope outward to open a channel for water molecules [85,88–90]. However, our results showed that the K40L mutant had little effect on the cytoplasmic side of helices B, D, and E (Figure 10D–F and Table S6), suggesting the main consequence of the mutant is to make sufficient preparations for the water chain required for the proton uptake. Our flashlight-induced transient absorption spectroscopy study on the native membrane of K40L-bR supported this proposal, showing shortened M-state decay and a shorter ground state recovery time (Figure S17). Additionally, it is worth noting that the apparent decrease in the intensity of the M state indicates that the proton pumping capacity of bR was weakened by the K40L mutant (Figure S17), which could be due to the more negative correlation caused by the K40L mutation (Figure S18).

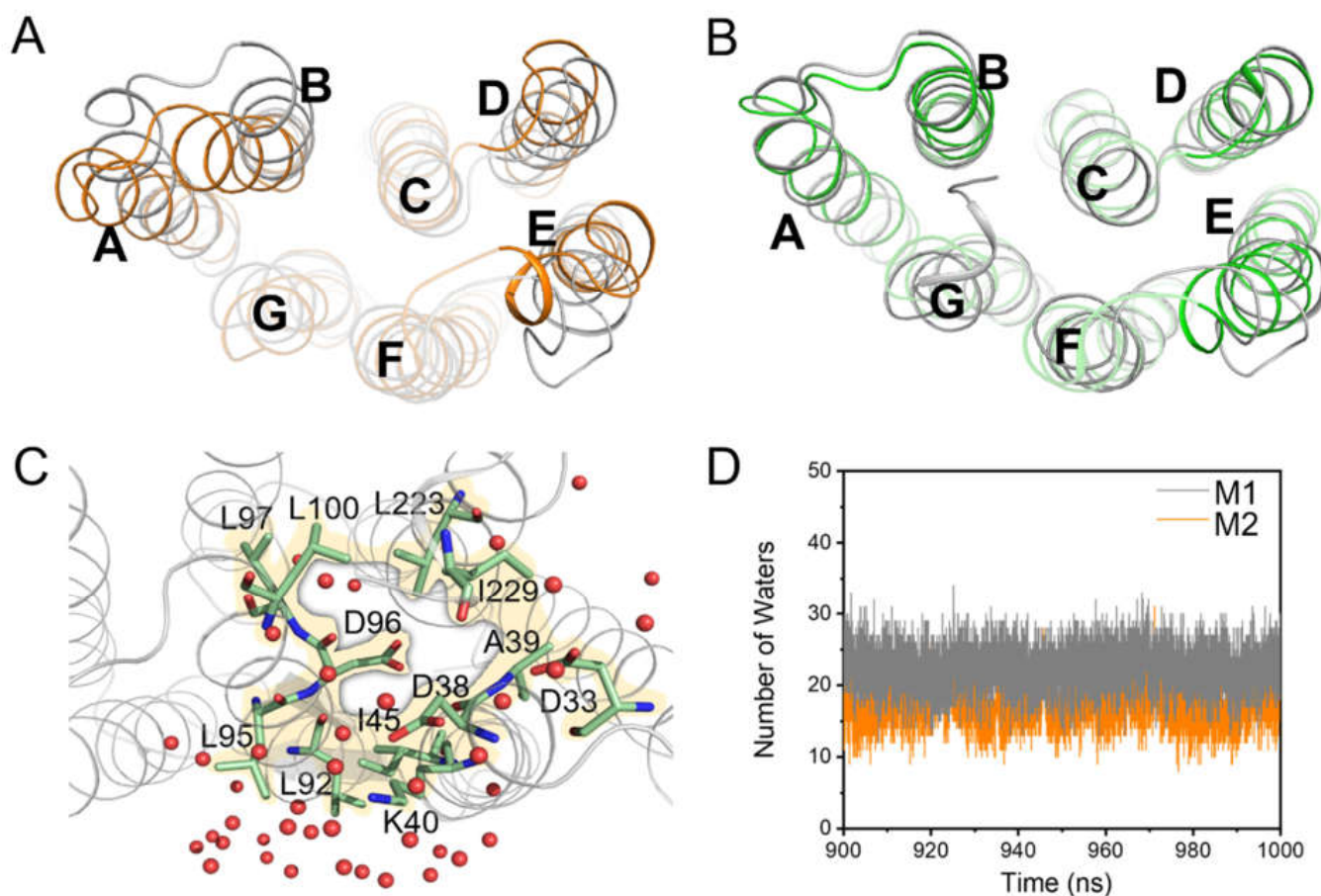


Figure 9. Dynamic changes in helices and water molecules on the cytoplasmic surface by the PGP-Me. (A) Superimposed drawing of the cytoplasmic side protein conformation of M1 (grey cartoon) and M2 (orange cartoon); (B) M1 and the late M state crystal structure of bR (PDB ID: 1FBB, green cartoon); (C) schematic diagram of the distribution of water molecules on the cytoplasmic surface from the last snapshot of M1. Red spheres represent the water molecules. D96 is surrounded by the key residues, especially hydrophobic ones (green stick and yellow surface). More water molecules gather around these residues, making it more accessible for them to enter the protein efficiently during the M state; (D) time series of the number of water molecules near the cytoplasmic surface in the last 100 ns simulations of M1 (grey line) and M2 (orange line).

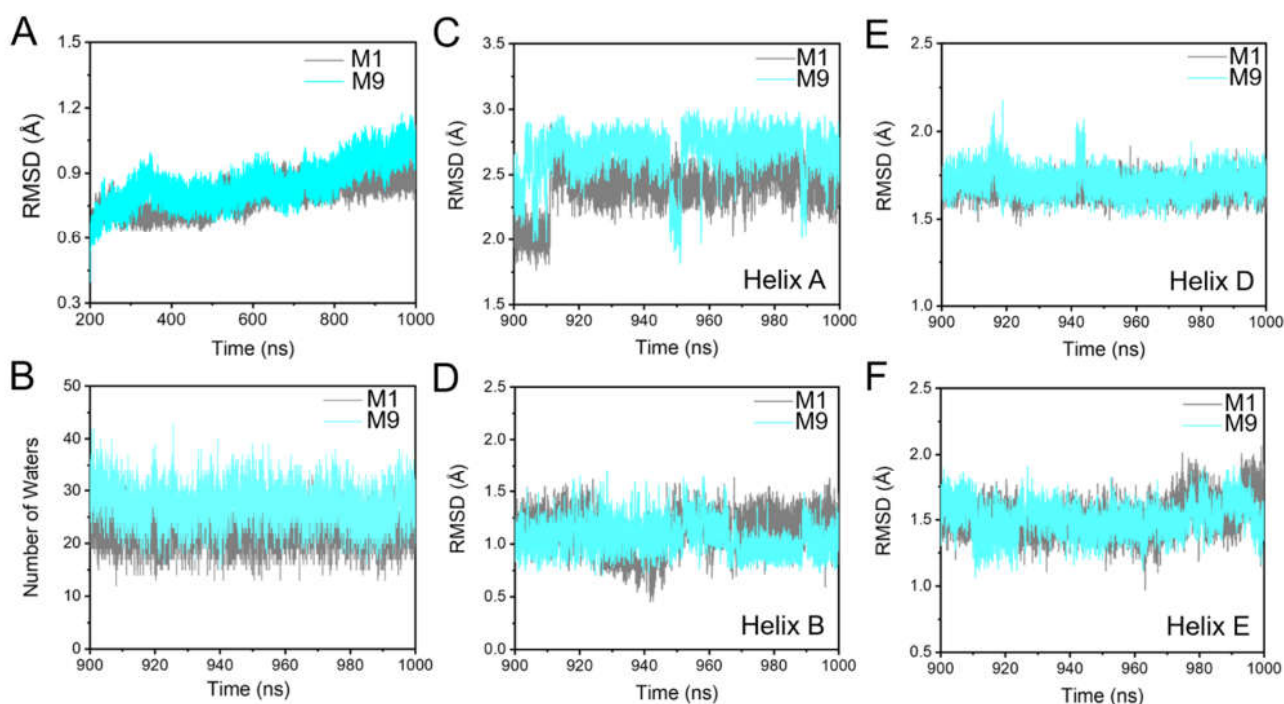


Figure 10. Dynamic changes in the helices and water molecules caused by the K40L mutation. (A) Time evolution of RMSD of the C α atoms during the simulation of M1 and M9 (membrane of the K40L-bR trimer with POPC, S-TGA-1, and PGP-Me); (B) time series of the number of water molecules near the cytoplasmic surface in the last 100 ns simulations of M1 and M9; (C–F) the RMSD of the cytoplasmic end of helices A (C), B (D), D (E), and E (F) in M1 and M9 in a late M-state crystal structure (PDB ID: 1FBB). A smaller RMSD indicates a larger opening. Grey and cyan indicate the M1 and M9, respectively.

3. Conclusions

For the first time, we provided detailed structural information about the specific interactions of S-TGA-1 and PGP-Me with bR. We demonstrated that these interactions promote the stability of the bR trimer and regulate proton transport by ensuring coherent conformation dynamics of bR and elucidated the underlying molecular mechanism by which key lipid–protein interactions affect proton uptake and release. On the extracellular side, W80 and K129 significantly influenced E194···E204 packing to form a “Glu-shared” model through interactions with S-TGA-1, making it conducive to facilitating proton release (Figure 11A). Removing those specific interactions in W80A and K129L disrupted the formation and decay of the photo-intermediate states, especially proton release, and further impeded the recovery of the ground state and the desensitization time (Figure S12). On the cytoplasmic side, the interaction between K40 and PGP-Me mainly affected bR photocycling by regulating the number of water molecules. The K40L mutation increased the number of water molecules around the hydrophobic residues, promoting faster proton uptake and shortening the photocycling lifetime (Figure 11B), which is the desired property for optogenetic tools [91,92].

This work demonstrates that the long-term and all-atom molecular dynamics simulation is a powerful method to connect the overall structural stability and conformational dynamics of a large membrane protein complex with the dynamic function of the protein. The strategy used here may be broadly applied to study the dynamic regulation of the function-related conformation changes induced by the specific binding of other membrane receptors, such as lipids or ligand bindings.

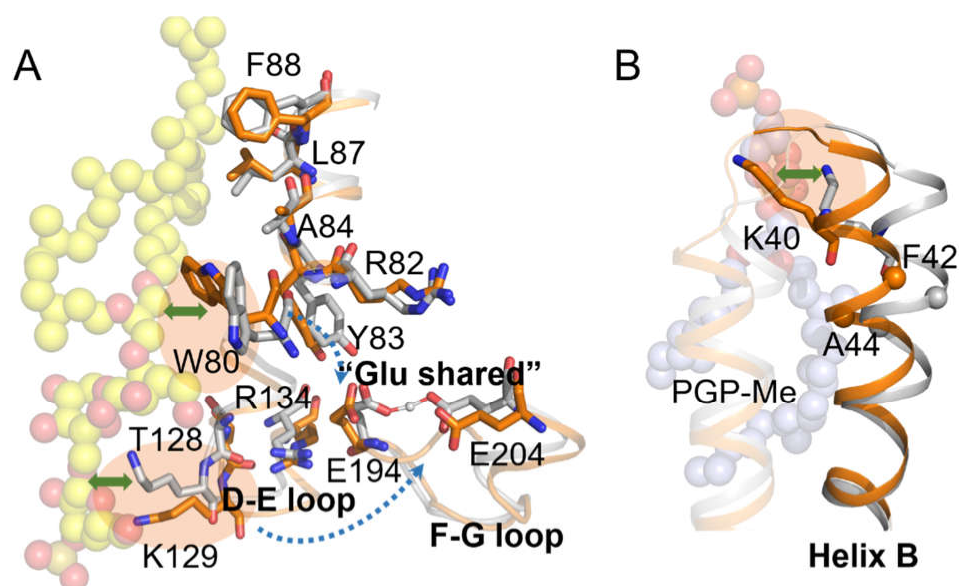


Figure 11. Schematic flowchart of the effects of S-TGA-1 (A) and PGP-Me (B) on the extracellular and cytoplasmic surfaces of bR. Yellow and light-blue spheres represent S-TGA-1 and PGP-Me, respectively. Grey and orange sticks indicate the regional conformation of bR and lipids in M1 and M2, respectively; green bidirectional arrows represent the specific interactions between residues and lipids, and blue dashed arrows indicate the regulatory role of W80 and K129 on the “Glu-shared” model.

4. Materials and Methods

4.1. Molecular Models and Parameters

The light-adapted state X-ray structure of bR with an all-*trans* retinal chromophore (PDB ID: 1C3W [75], with internal water) was used as a template in our calculations and simulations. For mutant simulations, we mutated the corresponding residues by PyMOL [69]. The CHARMM-GUI [93–96] server was used to build the initial structure of the simulations, including the explicitly hydrated bilayer, water molecules, and neutralized ions. As reported previously, the POPC (1-palmitoyl-2-oleoyl-sn-glycero-3-phosphocholine) lipid bilayer could reasonably maintain the interactions between residues in the bR trimer and the water dynamics [65,86,97–99] and its topology and parameters were tested extensively [100]. Therefore, all of our simulations (M1–M10) were performed in a POPC system constructed with 156 lipids (78 in the upper leaflet and 77 in the lower brochure) and about 10,000 water molecules. S-TGA-1 and PGP-Me were added to the corresponding positions in the bR trimer using TM-align [101] and PyMOL based on the information of GLC-1, MAN-2, SGA-3, ARC-1002, and GOL-1003 in 1BRR [32], and 2DP-267 in 2AT9 [35]. Each simulation system contained a bR trimer and 3 archaeal phospholipids S-TGA-1 and PGP-Me units. The missing residues in the loop regions of the crystal structure were built using the Schrödinger program [102], and the trimeric forms were generated from the symmetrical information of the crystal structures using VMD [103]. The position of the simulation model in the lipid membrane was determined by the PPM web server [70]. Asp96, Asp115, Glu204, and the Schiff base were protonated.

The retinal was treated as a single unit, and the parameters were obtained using the antechamber module and the general force field (GAFF) [104] in the AMBER program. Additionally, the parameters for S-TGA-1 and PGP-Me were obtained by combining Amber18 [67] and Gaussian16 [68]: First, we performed geometric optimization on S-TGA-1 and PGP-Me using the B3LYP/6-31G** level, and we then calculated the optimized structural singlet point energy, extracted the RESP2 charge [105], and fit the RESP2 charge and generated a small molecule force field file using the antechamber module in Amber18 [67]. The POPC lipid molecules were assigned to the Lipid14 force field [106]. The parameters of protein residues were assigned based on the AMBER ff14SB protein [107], and the TIP3P model [108] was utilized for the water molecules.

The final simulated systems were constructed using the XLEAP program [109]. MD simulations were carried out using the pmemd.cuda module in the AMBER18 program [67]. MD simulations with periodic boundary conditions were conducted in the NPT ensemble at 303 K and at 1 bar. Long-range electrostatic interactions were treated using the PME method [110], and empirical Lennard-Jones potentials were used to calculate the short-range van der Waals interactions with a cutoff of 10 Å. The temperature was regulated by Langevin dynamics [111] with a collision frequency of 1.0 ps⁻¹, the anisotropic Berendsen weak-coupling method [112] was utilized to couple the system to a barostat of 1 bar, and the SHAKE algorithm [113] was used to deal with the vibrations involving hydrogen atoms.

4.2. Molecular Dynamics Simulation

MD simulations were carried out using the pmemd.cuda module in the AMBER18 program [67]. First, we performed the simulations with everything fixed except the lipid tails to induce the appropriate disorder of a fluid-like bilayer. Then, we performed energy minimization and the equilibration of the bR-POPC (including bR-POPC-mutants) and bR-S-TGA-1_PGP-Me (including bR-S-TGA-1_PGP-Me-mutants) in two phases. Finally, the long-term unrestrained MD simulations continued when all of the atoms were free, and the coordinates were saved every 4 ps. The energy minimization and equilibration processes are described in detail below.

For the bR-S-TGA-1_PGP-Me and bR-S-TGA-1_PGP-Me-mutant simulations, each of the systems needed three-stage energy minimization. In the first stage, the protein, crystal water, and lipid bilayer (POPC) were restrained by a harmonic potential with a force constant of 10.0 kcal/mol·Å², S-TGA-1 and PGP-Me were controlled by a force constant of 30.0 kcal/mol·Å², and all of the other atoms were unrestrained; in the second stage, the protein, crystal water, and lipid bilayer (POPC) were restrained by a harmonic potential with a force constant of 5.0 kcal/mol·Å², S-TGA-1 and PGP-Me were controlled by a force constant of 20.0 kcal/mol·Å², and all of the other atoms were unrestrained; in the third stage, S-TGA-1 and PGP-Me were also restrained by a harmonic potential with a force constant of 20 kcal/mol·Å², and the remaining atoms were relaxed. Energy minimization was executed for 100,000 steps per stage, and the steepest descent method was used for the first 60,000 steps, which was then switched to the conjugate gradient method for the rest of the steps. After energy minimization, the whole system carried out three stages of equilibration. In the first stage, the systems were gradually heated from 0 to 100 K at 400 ps in the NVT ensemble, and the bR protein and crystal water were restrained by a harmonic potential with force constant of 10.0 kcal/mol·Å², S-TGA-1 and PGP-Me were restrained by a harmonic potential with a force constant of 100.0 kcal/mol·Å², and the lipid bilayer (POPC) was controlled by a force constant of 5.0 kcal/mol·Å²; in the next stage, the systems were gradually heated from 100 to 200 K at 400 ps in the NVT ensemble, and the bR protein and crystal water were restrained by a harmonic potential with a force constant of 8.0 kcal/mol·Å², S-TGA-1 and PGP-Me were restrained by a harmonic potential with force constant of 300.0 kcal/mol·Å², and the lipid bilayer (POPC) was controlled by a force constant of 2.5 kcal/mol·Å²; in the third stage, the systems were gradually heated from 200 to 303 K at 400 ps in the NVT ensemble, and the restraints of force constant on the bR protein and crystal waters reduced to 4.0 kcal/mol·Å², the force constant on the lipids (POPC) reduced to 2.0 kcal/mol·Å², and S-TGA-1 and PGP-Me were restrained by a harmonic potential with a force constant of 500.0 kcal/mol·Å². Then, we performed three 2 ns equilibrations with the NPT ensemble, where the constant pressure was 1.0 bar and where there were progressively decreasing force constant constraints on S-TGA-1 and PGP-Me, which, from first to last, were 300.0 kcal/mol·Å², 100.0 kcal/mol·Å², and 20.0 kcal/mol·Å².

For the bR-POPC and bR-POPC-mutant simulations, each system needed two-stage energy minimization. In the first stage, the protein, crystal water, and POPC were restrained by a harmonic potential with a force constant of 10.0 kcal/mol·Å², while all of the other atoms were unrestrained; in the second stage, all of the atoms were relaxed. Energy

minimization was executed for 100,000 steps per stage, and the steepest descent method was used for the first 50,000 steps, which was then switched to the conjugate gradient method for the rest of the steps. After energy minimization, the whole system carried out three equilibration stages. In the first stage, the systems were gradually heated from 0 to 100 K at 500 ps in the NVT ensemble, in which the bR protein and crystal water were restrained by a harmonic potential with a force constant of $5.0 \text{ kcal/mol}\cdot\text{\AA}^2$, and the POPC was controlled by a force constant of $2.5 \text{ kcal/mol}\cdot\text{\AA}^2$; in the next stage, the systems were gradually heated from 100 K to 303 K at 500 ps in the NVT ensemble, and the bR protein and crystal water were restrained by a harmonic potential with a force constant of $2.5 \text{ kcal/mol}\cdot\text{\AA}^2$, and the POPC was controlled by a force constant of $1.0 \text{ kcal/mol}\cdot\text{\AA}^2$; in the third stage, a 1 ns equilibration was performed at the NPT ensemble and at a constant temperature of 303 K, and the bR protein and crystal water were restrained by a harmonic potential with a force constant of $1.0 \text{ kcal/mol}\cdot\text{\AA}^2$, and the POPC was controlled by a force constant of $0.5 \text{ kcal/mol}\cdot\text{\AA}^2$. Then, we performed 10 ns unrestrained equilibrations with the NPT ensemble with the continuous pressure set at 1.0 bar.

4.3. Analysis of the Simulations

The cpptraj module of AmberTools18 was used to calculate the root mean square deviations (RMSD), root mean square fluctuation (RMSF), dynamic cross-correlation map (DCCM), the distances between key residues, the dihedral angle of the retinal, and the lifetime of the hydrogen bonds. The LigPlot+ diagrams [114] (including those for the hydrogen bonds and the van der Waals and hydrophobic interactions) were analyzed using HBPLUS [115] and LIGPLOT [116]. The dynamical cross-correlation networks were built based on the DCCM to represent the correlated motion between the residues in different domains. The $C\alpha$ atoms of each residue interacted with each other in the form of a pair of nodes [117], and PyMOL was used to visualize the interaction network. All molecular graphic and video representations were created using PyMOL.

Supplementary Materials: The following are available online at <https://www.mdpi.com/article/10.3390/ijms23136913/s1>, [118–130].

Author Contributions: Conceptualization, X.Z.; formal analysis, S.C. and X.D.; investigation, S.C., X.D., C.S., and F.W.; data curation, S.C.; writing—original draft preparation, S.C.; writing—review and editing, X.Z., X.D., S.C., A.W., and X.H.; supervision, X.Z.; funding acquisition, X.Z., A.W., and X.H. All authors have read and agreed to the published version of the manuscript.

Funding: This research was funded by the Natural Science Foundation of Shanghai Municipality (grant number 19ZR1416300), the Shanghai Pujiang Program (grant number 09PJ1404300), and the National Natural Science Foundation of China (grant numbers 30970657, 21475045, and 22074040) to X.Z.; the State Administration of Foreign Experts Affairs of China through the High-End Foreign Experts Recruitment Program (grant number GDW20123100086) to A.W.; the National Natural Science Foundation of China (grant numbers 21922301 and 21761132022), the National Key R&D Program of China (grant numbers 2019YFA0905200 and 2016YFA0501700), Shanghai Frontiers Science Center of Molecule Intelligent Syntheses, and the Fundamental Research Funds for the Central Universities to X.H. A.W. is a Leverhulme Fellow.

Institutional Review Board Statement: Not applicable.

Informed Consent Statement: Not applicable.

Data Availability Statement: Data related to this paper may be requested from the authors.

Acknowledgments: We thank the Supercomputer Centre of East China Normal University (ECNU Multifunctional Platform for Innovation 001).

Conflicts of Interest: The authors declare no conflict of interest.

Abbreviations

The following abbreviations are used in this manuscript:

M1	Membrane containing bR trimer, POPC, S-TGA-1, and PGP-Me lipids
M2	Membrane containing bR trimer and POPC lipids
M3	Membrane containing bR trimer, POPC, and S-TGA-1 lipids
M4	Membrane containing bR trimer, POPC, and PGP-Me lipids
M5	Membrane containing W80A-bR trimer, POPC, S-TGA-1, and PGP-Me lipids
M6	Membrane containing K129L-bR trimer, POPC, S-TGA-1, and PGP-Me lipids
M7	Membrane containing W80A-bR trimer and POPC lipids
M8	Membrane containing K129L-bR trimer and POPC lipids
M9	Membrane containing K40L-bR trimer, POPC, S-TGA-1, and PGP-Me lipids
M10	Membrane containing K40L-bR trimer and POPC lipids

References

- Overington, J.P.; Al-Lazikani, B.; Hopkins, A.L. How many drug targets are there? *Nat. Rev. Drug Discov.* **2006**, *5*, 993–996. [[CrossRef](#)] [[PubMed](#)]
- Yin, H.; Flynn, A.D. Drugging Membrane Protein Interactions. *Annu. Rev. Biomed. Eng.* **2016**, *18*, 51–76. [[CrossRef](#)]
- Hancock, J.F. Lipid rafts: Contentious only from simplistic standpoints. *Nat. Rev. Mol. Cell Biol.* **2006**, *7*, 456–462. [[CrossRef](#)] [[PubMed](#)]
- van Meer, G.; Voelker, D.R.; Feigenson, G.W. Membrane lipids: Where they are and how they behave. *Nat. Rev. Mol. Cell Biol.* **2008**, *9*, 112–124. [[CrossRef](#)]
- Nishimura, T.; Tooze, S.A. Emerging roles of ATG proteins and membrane lipids in autophagosome formation. *Cell Discov.* **2020**, *6*, 32. [[CrossRef](#)]
- Janmey, P.A.; Kinnunen, P.K.J. Biophysical properties of lipids and dynamic membranes. *Trends Cell Biol.* **2006**, *16*, 538–546. [[CrossRef](#)] [[PubMed](#)]
- Laganowsky, A.; Reading, E.; Allison, T.M.; Ulmschneider, M.B.; Degiacomi, M.T.; Baldwin, A.J.; Robinson, C.V. Membrane proteins bind lipids selectively to modulate their structure and function. *Nature* **2014**, *510*, 172–175. [[CrossRef](#)]
- Yen, H.-Y.; Hoi, K.K.; Liko, I.; Hedger, G.; Horrell, M.R.; Song, W.; Wu, D.; Heine, P.; Warne, T.; Lee, Y.; et al. PtdIns(4,5)P₂ stabilizes active states of GPCRs and enhances selectivity of G-protein coupling. *Nature* **2018**, *559*, 423–427. [[CrossRef](#)]
- Lee, A.G. Lipid-protein interactions in biological membranes: A structural perspective. *Biochim. Biophys. Acta* **2003**, *1612*, 1–40. [[CrossRef](#)]
- Lee, A.G. Lipid-protein interactions. *Biochem. Soc. Trans.* **2011**, *39*, 761–766. [[CrossRef](#)]
- Weingarth, M.; Prokofyev, A.; van der Cruisen, E.A.W.; Nand, D.; Bonvin, A.M.J.J.; Pongs, O.; Baldus, M. Structural Determinants of Specific Lipid Binding to Potassium Channels. *J. Am. Chem. Soc.* **2013**, *135*, 3983–3988. [[CrossRef](#)]
- Schmidt, D.; Jiang, Q.-X.; MacKinnon, R. Phospholipids and the origin of cationic gating charges in voltage sensors. *Nature* **2006**, *444*, 775–779. [[CrossRef](#)]
- Domene, C.; Bond, P.J.; Deol, S.S.; Sansom, M.S.P. Lipid/Protein Interactions and the Membrane/Water Interfacial Region. *J. Am. Chem. Soc.* **2003**, *125*, 14966–14967. [[CrossRef](#)]
- Sansom, M.S.; Bond, P.J.; Deol, S.S.; Grottesi, A.; Haider, S.; Sands, Z.A. Molecular simulations and lipid-protein interactions: Potassium channels and other membrane proteins. *Biochem. Soc. Trans.* **2005**, *33*, 916–920. [[CrossRef](#)]
- Duncan, A.L.; Song, W.; Sansom, M.S.P. Lipid-Dependent Regulation of Ion Channels and G Protein-Coupled Receptors: Insights from Structures and Simulations. *Annu. Rev. Pharmacol. Toxicol.* **2020**, *60*, 31–50. [[CrossRef](#)]
- Zhou, Y.; Morais-Cabral, J.H.; Kaufman, A.; MacKinnon, R. Chemistry of ion coordination and hydration revealed by a K⁺ channel-Fab complex at 2.0 Å resolution. *Nature* **2001**, *414*, 43–48. [[CrossRef](#)]
- Belrhali, H.; Nollert, P.; Royant, A.; Menzel, C.; Rosenbusch, J.; Landau, E.; Pebay-Peyroula, E. Protein, lipid and water organization in bacteriorhodopsin crystals: A molecular view of the purple membrane at 1.9 Å resolution. *Structure* **1999**, *7*, 909–917. [[CrossRef](#)]
- Cartailler, J.-P.; Luecke, H. X-Ray Crystallographic Analysis of Lipid-Protein Interactions in the Bacteriorhodopsin Purple Membrane. *Annu. Rev. Biophys. Biomol. Struct.* **2003**, *32*, 285–310. [[CrossRef](#)]
- Oesterhelt, D.; Stoekenius, W. Rhodopsin-like Protein from the Purple Membrane of Halobacterium halobium. *Nat. New Biol.* **1971**, *233*, 149–152. [[CrossRef](#)]
- Ernst, O.; Lodowski, D.; Elstner, M.; Hegemann, P.; Brown, L.; Kandori, H. Microbial and Animal Rhodopsins: Structures, Functions, and Molecular Mechanisms. *Chem. Rev.* **2013**, *114*, 126–163. [[CrossRef](#)]
- Oesterhelt, D.; Stoekenius, W. Functions of a new photoreceptor membrane. *Proc. Natl. Acad. Sci. USA* **1973**, *70*, 2853–2857. [[CrossRef](#)] [[PubMed](#)]
- Stoekenius, W.; Lozier, R.H.; Bogomolni, R.A. Bacteriorhodopsin and the purple membrane of halobacteria. *Biochim. Biophys. Acta* **1979**, *505*, 215–278. [[CrossRef](#)]
- Kühlbrandt, W. Bacteriorhodopsin—The movie. *Nature* **2000**, *406*, 569–570. [[CrossRef](#)] [[PubMed](#)]

24. Lanyi, J.K. Bacteriorhodopsin. *Annu. Rev. Physiol.* **2004**, *66*, 665–688. [[CrossRef](#)]
25. Lanyi, J.K. Mechanism of proton transport from crystallographic structures of the nine states of the bacteriorhodopsin photocycle. *Biochim. Biophys. Acta* **2004**, *1658*, 78.
26. Wickstrand, C.; Nogly, P.; Nango, E.; Iwata, S.; Standfuss, J.; Neutze, R. Bacteriorhodopsin: Structural Insights Revealed Using X-Ray Lasers and Synchrotron Radiation. *Annu. Rev. Biochem.* **2019**, *88*, 59–83. [[CrossRef](#)]
27. Lanyi, J.K.; Schobert, B. Mechanism of Proton Transport in Bacteriorhodopsin from Crystallographic Structures of the K, L, M1, M2, and M2' Intermediates of the Photocycle. *J. Mol. Biol.* **2003**, *328*, 439–450. [[CrossRef](#)]
28. Corcelli, A.; Colella, M.; Mascolo, G.; Fanizzi, F.P.; Kates, M. A Novel Glycolipid and Phospholipid in the Purple Membrane. *Biochemistry* **2000**, *39*, 3318–3326. [[CrossRef](#)]
29. Corcelli, A.; Lattanzio, V.M.T.; Mascolo, G.; Papadia, P.; Fanizzi, F. Lipid-protein stoichiometries in a crystalline biological membrane: NMR quantitative analysis of the lipid extract of the purple membrane. *J. Lipid Res.* **2002**, *43*, 132–140. [[CrossRef](#)]
30. Renner, C.; Kessler, B.; Oesterhelt, D. Lipid composition of integral purple membrane by ¹H and ³¹P NMR. *J. Lipid Res.* **2005**, *46*, 1755–1764. [[CrossRef](#)]
31. Kushwaha, S.C.; Kates, M.; Martin, W.G. Characterization and composition of the purple and red membrane from *Halobacterium cutirubrum*. *Can. J. Biochem.* **1975**, *53*, 284–292. [[CrossRef](#)]
32. Essen, L.; Siegert, R.; Lehmann, W.D.; Oesterhelt, D. Lipid patches in membrane protein oligomers: Crystal structure of the bacteriorhodopsin-lipid complex. *Proc. Natl. Acad. Sci. USA* **1998**, *95*, 11673–11678. [[CrossRef](#)]
33. Dracheva, S.; Bose, S.; Hendler, R.W. Chemical and functional studies on the importance of purple membrane lipids in bacteriorhodopsin photocycle behavior. *FEBS Lett.* **1996**, *382*, 209–212. [[CrossRef](#)]
34. Watts, A. Bacteriorhodopsin: The mechanism of 2D-array formation and the structure of retinal in the protein. *Biophys. Chem.* **1995**, *55*, 137–151. [[CrossRef](#)]
35. Mitsuoka, K.; Hirai, T.; Murata, K.; Miyazawa, A.; Kidera, A.; Kimura, Y.; Fujiyoshi, Y. The structure of bacteriorhodopsin at 3.0 Å resolution based on electron crystallography: Implication of the charge distribution. *J. Mol. Biol.* **1999**, *286*, 861–882. [[CrossRef](#)]
36. Sternberg, B.; L'Hostis, C.; Whiteway, C.A.; Watts, A. The essential role of specific *Halobacterium halobium* polar lipids in 2D-array formation of bacteriorhodopsin. *Biochim. Biophys. Acta* **1992**, *1108*, 21–30. [[CrossRef](#)]
37. Bryl, K.; Yoshihara, K. The role of retinal in the long-range protein-lipid interactions in bacteriorhodopsin-phosphatidylcholine vesicles. *Eur. Biophys. J. Biophys.* **2001**, *29*, 628–640. [[CrossRef](#)]
38. Cui, J.; Kawatake, S.; Umegawa, Y.; Lethu, S.; Yamagami, M.; Matsuoka, S.; Sato, F.; Matsumori, N.; Murata, M. Stereoselective synthesis of the head group of archaeal phospholipid PGP-Me to investigate bacteriorhodopsin-lipid interactions. *Org. Biomol. Chem.* **2015**, *13*, 10279–10284. [[CrossRef](#)]
39. Hendler, R.W.; Barnett, S.M.; Dracheva, S.; Bose, S.; Levin, I.W. Purple membrane lipid control of bacteriorhodopsin conformational flexibility and photocycle activity. *Eur. J. Biochem.* **2003**, *270*, 1920–1925. [[CrossRef](#)]
40. Hendler, R.W.; Dracheva, S. Importance of Lipids for Bacteriorhodopsin Structure, Photocycle, and Function. *Biochemistry* **2001**, *66*, 1311–1314. [[CrossRef](#)]
41. Mukhopadhyay, A.K.; Bose, S.; Hendler, R.W. Membrane-Mediated Control of the Bacteriorhodopsin Photocycle. *Biochemistry* **1994**, *33*, 10889–10895. [[CrossRef](#)] [[PubMed](#)]
42. Mukhopadhyay, A.K.; Dracheva, S.; Bose, S.; Hendler, R.W. Control of the Integral Membrane Proton Pump, Bacteriorhodopsin, by Purple Membrane Lipids of *Halobacterium halobium*. *Biochemistry* **1996**, *35*, 9245–9252. [[CrossRef](#)] [[PubMed](#)]
43. Höjberg, B.; Lind, C.; Khorana, H.G. Reconstitution of bacteriorhodopsin vesicles with *Halobacterium halobium* lipids. Effects of variations in lipid composition. *J. Biol. Chem.* **1982**, *257*, 1690–1694. [[CrossRef](#)]
44. Joshi, M.K.; Dracheva, S.; Mukhopadhyay, A.K.; Bose, S.; Hendler, R.W. Importance of Specific Native Lipids in Controlling the Photocycle of Bacteriorhodopsin. *Biochemistry* **1998**, *37*, 14463–14470. [[CrossRef](#)] [[PubMed](#)]
45. Gonzalez-Manas, J.M.; Virto, M.D.; Gurtubay, J.I.; Goni, F.M. The interaction of Triton X-100 with purple membranes. Detergent binding, spectral changes and membrane solubilization. *Eur. J. Biochem.* **1990**, *188*, 673–678. [[CrossRef](#)] [[PubMed](#)]
46. Gonzalez-Manas, J.M.; Goni, F.M.; Tribout, M.; Paredes, S. Kinetics of purple membrane dark-adaptation in the presence of Triton X-100. *Arch. Biochem. Biophys.* **1990**, *282*, 239–243. [[CrossRef](#)]
47. Hu, K.; Sun, Y.; Chen, D.; Zhang, Y. The effect of lipid environment in purple membrane on bacteriorhodopsin. *J. Photochem. Photobiol. B Biol.* **2000**, *58*, 163–169. [[CrossRef](#)]
48. Lopez, F.; Lobasso, S.; Colella, M.; Agostiano, A.; Corcelli, A. Light-dependent and Biochemical Properties of Two Different Bands of Bacteriorhodopsin Isolated on Phenyl-Sepharose CL-4B. *Photochem. Photobiol.* **1999**, *69*, 599–604. [[CrossRef](#)]
49. Weik, M.; Patzelt, H.; Zaccai, G.; Oesterhelt, D. Localization of Glycolipids in Membranes by In Vivo Labeling and Neutron Diffraction. *Mol. Cell* **1998**, *1*, 411–419. [[CrossRef](#)]
50. Barnett, S.M.; Dracheva, S.; Hendler, R.W.; Levin, I.W. Lipid-Induced Conformational Changes of an Integral Membrane Protein: An Infrared Spectroscopic Study of the Effects of Triton X-100 Treatment on the Purple Membrane of *Halobacterium halobium* ET1001. *Biochemistry* **1996**, *35*, 4558–4567. [[CrossRef](#)]
51. Milder, S.J.; Thorgeirsson, T.E.; Miercke, L.J.W.; Stroud, R.M.; Kliger, D.S. Effects of detergent environments on the photocycle of purified monomeric bacteriorhodopsin. *Biochemistry* **1991**, *30*, 1751–1761. [[CrossRef](#)]
52. Inada, M.; Kinoshita, M.; Matsumori, N. Archaeal Glycolipid S-TGA-1 Is Crucial for Trimer Formation and Photocycle Activity of Bacteriorhodopsin. *ACS Chem. Biol.* **2020**, *15*, 197–204. [[CrossRef](#)]

53. Inada, M.; Kinoshita, M.; Sumino, A.; Oiki, S.; Matsumori, N. A concise method for quantitative analysis of interactions between lipids and membrane proteins. *Anal. Chim. Acta* **2019**, *1059*, 103–112. [[CrossRef](#)]
54. Matsui, Y.; Sakai, K.; Murakami, M.; Shiro, Y.; Adachi, S.-I.; Okumura, H.; Kouyama, T. Specific Damage Induced by X-ray Radiation and Structural Changes in the Primary Photoreaction of Bacteriorhodopsin. *J. Mol. Biol.* **2002**, *324*, 469–481. [[CrossRef](#)]
55. Sato, H.; Takeda, K.; Tani, K.; Hino, T.; Okada, T.; Nakasako, M.; Kamiya, N.; Kouyama, T. Specific lipid-protein interactions in a novel honeycomb lattice structure of bacteriorhodopsin. *Acta Crystallogr. D Biol. Crystallogr.* **1999**, *55*, 1251–1256. [[CrossRef](#)]
56. Muller, M.P.; Jiang, T.; Sun, C.; Lihan, M.; Pant, S.; Mahinthichaichan, P.; Trifan, A.; Tajkhorshid, E. Characterization of Lipid-Protein Interactions and Lipid-Mediated Modulation of Membrane Protein Function through Molecular Simulation. *Chem. Rev.* **2019**, *119*, 6086–6161. [[CrossRef](#)]
57. Gu, R.-X.; de Groot, B.L. Lipid-protein interactions modulate the conformational equilibrium of a potassium channel. *Nat. Commun* **2020**, *11*, 2162. [[CrossRef](#)]
58. Yang, J.; Aslimovska, L.; Glaubitz, C. Molecular Dynamics of Proteorhodopsin in Lipid Bilayers by Solid-State NMR. *J. Am. Chem. Soc.* **2011**, *133*, 4874–4881. [[CrossRef](#)]
59. Agasid, M.T.; Robinson, C.V. Probing membrane protein–lipid interactions. *Curr. Opin. Struct. Biol.* **2021**, *69*, 78–85. [[CrossRef](#)]
60. Corradi, V.; Sejdiu, B.I.; Mesa-Galoso, H.; Abdizadeh, H.; Noskov, S.Y.; Marrink, S.J.; Tieleman, D.P. Emerging Diversity in Lipid-Protein Interactions. *Chem. Rev.* **2019**, *119*, 5775–5848. [[CrossRef](#)]
61. Duncan, A.; Corey, R.; Sansom, M. Defining how multiple lipid species interact with inward rectifier potassium (Kir2) channels. *Proc. Natl. Acad. Sci. USA* **2020**, *117*, 7803–7813. [[CrossRef](#)] [[PubMed](#)]
62. Amos, S.T.A.; Kalli, A.C.; Shi, J.; Sansom, M.S.P. Membrane Recognition and Binding by the Phosphatidylinositol Phosphate Kinase PIP5K1A: A Multiscale Simulation Study. *Structure* **2019**, *27*, 1336–1346. [[CrossRef](#)] [[PubMed](#)]
63. Chavent, M.; Duncan, A.L.; Sansom, M.S.P. Molecular dynamics simulations of membrane proteins and their interactions: From nanoscale to mesoscale. *Curr. Opin. Struct. Biol.* **2016**, *40*, 8–16. [[CrossRef](#)] [[PubMed](#)]
64. Jang, H.; Crozier, P.S.; Stevens, M.J.; Woolf, T.B. How Environment Supports a State: Molecular Dynamics Simulations of Two States in Bacteriorhodopsin Suggest Lipid and Water Compensation. *Biophys. J.* **2004**, *87*, 129–145. [[CrossRef](#)] [[PubMed](#)]
65. Kandt, C.; Gerwert, K.; Schlitter, J. Water dynamics simulation as a tool for probing proton transfer pathways in a heptahelical membrane protein. *Proteins Struct. Funct. Bioinform.* **2005**, *58*, 528–537. [[CrossRef](#)]
66. Tieleman, D.; Berendsen, H.; Sansom, M. An Alamethicin Channel in a Lipid Bilayer: Molecular Dynamics Simulations. *Biophys. J.* **1999**, *76*, 1757–1769. [[CrossRef](#)]
67. Case, D.A.; Betz, R.; Cerutti, D.; Cheatham, T.E.; Darden, T.; Duke, R.; Giese, T.J.; Gohlke, H.; Götz, A.; Homeyer, N. *Amber 2018*; University of California: San Francisco, CA, USA, 2018. [[CrossRef](#)]
68. Frisch, M.J.; Trucks, G.W.; Schlegel, H.B.; Scuseria, G.E.; Robb, M.A. *Gaussian 16*; Gaussian Inc.: Wallingford, CT, USA, 2016.
69. DeLano, W.L. *The PyMOL Molecular Graphics System*; Delano Scientific: San Carlos, CA, USA, 2002.
70. Lomize, M.A.; Pogozheva, I.D.; Joo, H.; Mosberg, H.I.; Lomize, A.L. OPM database and PPM web server: Resources for positioning of proteins in membranes. *Nucleic Acids Res.* **2012**, *40*, D370–D376. [[CrossRef](#)]
71. Mayer, K.L.; Earley, M.R.; Gupta, S.; Pichumani, K.; Regan, L.; Stone, M.J. Covariation of backbone motion throughout a small protein domain. *Nat. Struct. Biol.* **2003**, *10*, 962–965. [[CrossRef](#)]
72. Lange, O.F.; Grubmüller, H.; de Groot, B.L. Molecular Dynamics Simulations of Protein G Challenge NMR-Derived Correlated Backbone Motions. *Angew. Chem. Int. Ed.* **2005**, *44*, 3394–3399. [[CrossRef](#)]
73. Ghosh, A.; Vishveshwara, S. A study of communication pathways in methionyl- tRNA synthetase by molecular dynamics simulations and structure network analysis. *Proc. Natl. Acad. Sci. USA* **2007**, *104*, 15711–15716. [[CrossRef](#)]
74. Kumari, M.; Singh, R.; Subbarao, N. Exploring the interaction mechanism between potential inhibitor and multi-target Mur enzymes of mycobacterium tuberculosis using molecular docking, molecular dynamics simulation, principal component analysis, free energy landscape, dynamic cross-correlation matrices, vector movements, and binding free energy calculation. *J. Biomol. Struct. Dyn.* **2021**, 1–30. [[CrossRef](#)]
75. Luecke, H.; Schobert, B.; Richter, H.-T.; Cartailler, J.-P.; Lanyi, J.K. Structure of bacteriorhodopsin at 1.55 Å resolution. *J. Mol. Biol.* **1999**, *291*, 899–911. [[CrossRef](#)]
76. Wolf, S.; Freier, E.; Gerwert, K. A delocalized proton-binding site within a membrane protein. *Biophys. J.* **2014**, *107*, 174–184. [[CrossRef](#)]
77. Goyal, P.; Ghosh, N.; Phatak, P.; Clemens, M.; Gaus, M.; Elstner, M.; Cui, Q. Proton storage site in bacteriorhodopsin: New insights from quantum mechanics/molecular mechanics simulations of microscopic pKa and infrared spectra. *J. Am. Chem. Soc.* **2011**, *133*, 14981–14997. [[CrossRef](#)]
78. Phatak, P.; Ghosh, N.; Yu, H.; Cui, Q.; Elstner, M. Amino acids with an intermolecular proton bond as proton storage site in bacteriorhodopsin. *Proc. Natl. Acad. Sci. USA* **2008**, *105*, 19672–19677. [[CrossRef](#)]
79. Tripathi, R.; Forbert, H.; Marx, D. Settling the Long-Standing Debate on the Proton Storage Site of the Prototype Light-Driven Proton Pump Bacteriorhodopsin. *J. Phys. Chem. B* **2019**, *123*, 9598–9608. [[CrossRef](#)]
80. Nakai, H.; Takemura, T.; Ono, J.; Nishimura, Y. Quantum-Mechanical Molecular Dynamics Simulations on Secondary Proton Transfer in Bacteriorhodopsin Using Realistic Models. *J. Phys. Chem. B* **2021**, *125*, 10947–10963. [[CrossRef](#)]
81. Clemens, M.; Phatak, P.; Cui, Q.; Bondar, A.-N.; Elstner, M. Role of Arg82 in the Early Steps of the Bacteriorhodopsin Proton-Pumping Cycle. *J. Phys. Chem. B* **2011**, *115*, 7129–7135. [[CrossRef](#)]

82. Govindjee, R.; Imasheva, E.S.; Misra, S.; Balashov, S.P.; Ebrey, T.G.; Chen, N.; Menick, D.R.; Crouch, R.K. Mutation of a Surface Residue, Lysine-129, Reverses the Order of Proton Release and Uptake in Bacteriorhodopsin; Guanidine Hydrochloride Restores It. *Biophys. J.* **1997**, *72*, 886–898. [[CrossRef](#)]
83. Lórenz-Fonfría, V.A.; Furutani, Y.; Kandori, H. Active Internal Waters in the Bacteriorhodopsin Photocycle. A Comparative Study of the L and M Intermediates at Room and Cryogenic Temperatures by Infrared Spectroscopy. *Biochemistry* **2008**, *47*, 4071–4081. [[CrossRef](#)]
84. Dioumaev, A.K.; Brown, L.S.; Needleman, R.; Lanyi, J.K. Partitioning of free energy gain between the photoisomerized retinal and the protein in bacteriorhodopsin. *Biochemistry* **1998**, *37*, 9889–9893. [[CrossRef](#)] [[PubMed](#)]
85. Weinert, T.; Skopintsev, P.; James, D.; Dworkowski, F.; Panepucci, E.; Kekilli, D.; Furrer, A.; Brünle, S.; Mous, S.; Ozerov, D.; et al. Proton uptake mechanism in bacteriorhodopsin captured by serial synchrotron crystallography. *Science* **2019**, *365*, 61–65. [[CrossRef](#)] [[PubMed](#)]
86. Freier, E.; Wolf, S.; Gerwert, K. Proton transfer via a transient linear water-molecule chain in a membrane protein. *Proc. Natl. Acad. Sci. USA* **2011**, *108*, 11435–11439. [[CrossRef](#)] [[PubMed](#)]
87. Otomo, J.; Tomioka, H.; Sasabe, H. Properties and the primary structure of a new halorhodopsin from halobacterial strain mex. *Biochim. Biophys. Acta* **1992**, *1112*, 7–13. [[CrossRef](#)]
88. Chen, D.; Lanyi, J.K. Structural changes in the N and N' states of the bacteriorhodopsin photocycle. *Biophys. J.* **2009**, *96*, 2779–2788. [[CrossRef](#)]
89. Shibata, M.; Yamashita, H.; Uchihashi, T.; Kandori, H.; Ando, T. High-speed atomic force microscopy shows dynamic molecular processes in photoactivated bacteriorhodopsin. *Nat. Nanotechnol.* **2010**, *5*, 208–212. [[CrossRef](#)]
90. Luecke, H.; Schobert, B.; Richter, H.T.; Cartailler, J.P.; Lanyi, J.K. Structural Changes in Bacteriorhodopsin During Ion Transport at 2 Angstrom Resolution. *Science* **1999**, *286*, 255–260. [[CrossRef](#)]
91. Kato, H.E.; Kamiya, M.; Sugo, S.; Ito, J.; Taniguchi, R.; Orito, A.; Hirata, K.; Inutsuka, A.; Yamanaka, A.; Maturana, A.D.; et al. Atomistic design of microbial opsin-based blue-shifted optogenetics tools. *Nat. Commun.* **2015**, *6*, 7177. [[CrossRef](#)]
92. Inoue, K. *Diversity, Mechanism, and Optogenetic Application of Light-Driven Ion Pump Rhodopsins*; Springer: Singapore, 2021; pp. 89–126. [[CrossRef](#)]
93. Jo, S.; Kim, T.; Im, W. Automated Builder and Database of Protein/Membrane Complexes for Molecular Dynamics Simulations. *PLoS ONE* **2007**, *2*, e880. [[CrossRef](#)]
94. Jo, S.; Kim, T.; Iyer, V.G.; Im, W. CHARMM-GUI: A web-based graphical user interface for CHARMM. *J. Comput. Chem.* **2008**, *29*, 1859–1865. [[CrossRef](#)]
95. Jo, S.; Lim, J.B.; Klauda, J.B.; Im, W. CHARMM-GUI Membrane Builder for Mixed Bilayers and Its Application to Yeast Membranes. *Biophys. J.* **2009**, *97*, 50–58. [[CrossRef](#)]
96. Lee, J.; Cheng, X.; Swails, J.M.; Yeom, M.S.; Eastman, P.K.; Lemkul, J.A.; Wei, S.; Buckner, J.; Jeong, J.C.; Qi, Y.; et al. CHARMM-GUI Input Generator for NAMD, GROMACS, AMBER, OpenMM, and CHARMM/OpenMM Simulations Using the CHARMM36 Additive Force Field. *J. Chem. Theory Comput.* **2016**, *12*, 405–413. [[CrossRef](#)]
97. Kandt, C.; Schlitter, J.; Gerwert, K. Dynamics of Water Molecules in the Bacteriorhodopsin Trimer in Explicit Lipid/Water Environment. *Biophys. J.* **2004**, *86*, 705–717. [[CrossRef](#)]
98. Grudinin, S.; Büldt, G.; Gordeliy, V.; Baumgaertner, A. Water Molecules and Hydrogen-Bonded Networks in Bacteriorhodopsin—Molecular Dynamics Simulations of the Ground State and the M-Intermediate. *Biophys. J.* **2005**, *88*, 3252–3261. [[CrossRef](#)]
99. del Val, C.; Bondar, L.; Bondar, A.-N. Coupling between inter-helical hydrogen bonding and water dynamics in a proton transporter. *J. Struct. Biol.* **2014**, *186*, 95–111. [[CrossRef](#)]
100. Feller, S.E.; MacKerell, A.D. An Improved Empirical Potential Energy Function for Molecular Simulations of Phospholipids. *J. Phys. Chem. B* **2000**, *104*, 7510–7515. [[CrossRef](#)]
101. Zhang, Y.; Skolnick, J. TM-align: A protein structure alignment algorithm based on the TM-score. *Nucleic Acids Res.* **2005**, *33*, 2302–2309. [[CrossRef](#)]
102. Schrödinger, LLC. *Schrödinger Suites*; Schrödinger, LLC: New York, NY, USA, 2015.
103. Humphrey, W.; Dalke, A.; Schulten, K. VMD: Visual molecular dynamics. *J. Mol. Graph.* **1996**, *14*, 33–38. [[CrossRef](#)]
104. Wang, J.; Wolf, R.M.; Caldwell, J.W.; Kollman, P.A.; Case, D.A. Development and testing of a general amber force field. *J. Comput. Chem.* **2004**, *25*, 1157–1174. [[CrossRef](#)]
105. Schauerperl, M.; Nerenberg, P.S.; Jang, H.; Wang, L.-P.; Bayly, C.I.; Mobley, D.L.; Gilson, M.K. Non-bonded force field model with advanced restrained electrostatic potential charges (RESP2). *Commun. Chem.* **2020**, *3*, 44. [[CrossRef](#)]
106. Dickson, C.J.; Madej, B.D.; Skjevik, Å.A.; Betz, R.M.; Teigen, K.; Gould, I.R.; Walker, R.C. Lipid14: The Amber Lipid Force Field. *J. Chem. Theory Comput.* **2014**, *10*, 865–879. [[CrossRef](#)] [[PubMed](#)]
107. Maier, J.A.; Martinez, C.; Kasavajhala, K.; Wickstrom, L.; Hauser, K.E.; Simmerling, C. ff14SB: Improving the Accuracy of Protein Side Chain and Backbone Parameters from ff99SB. *J. Chem. Theory Comput.* **2015**, *11*, 3696–3713. [[CrossRef](#)] [[PubMed](#)]
108. Jorgensen, W.L.; Chandrasekhar, J.; Madura, J.D.; Impey, R.W.; Klein, M.L. Comparison of simple potential functions for simulating liquid water. *J. Chem. Phys.* **1983**, *79*, 926–935. [[CrossRef](#)]
109. Pearlman, D.A.; Case, D.A.; Caldwell, J.W.; Ross, W.S.; Cheatham, T.E.; DeBolt, S.; Ferguson, D.; Seibel, G.; Kollman, P. AMBER, a package of computer programs for applying molecular mechanics, normal mode analysis, molecular dynamics and free energy calculations to simulate the structural and energetic properties of molecules. *Comput. Phys. Commun.* **1995**, *91*, 1–41. [[CrossRef](#)]

110. Darden, T.; York, D.; Pedersen, L. Particle mesh Ewald: An N·log(N) method for Ewald sums in large systems. *J. Chem. Phys.* **1993**, *98*, 10089–10092. [[CrossRef](#)]
111. Cerutti, D.S.; Duke, R.; Freddolino, P.L.; Fan, H.; Lybrand, T.P. A Vulnerability in Popular Molecular Dynamics Packages Concerning Langevin and Andersen Dynamics. *J. Chem. Theory Comput.* **2008**, *4*, 1669–1680. [[CrossRef](#)]
112. Berendsen, H.J.C.; Postma, J.P.M.; van Gunsteren, W.F.; DiNola, A.; Haak, J.R. Molecular dynamics with coupling to an external bath. *J. Chem. Phys.* **1984**, *81*, 3684–3690. [[CrossRef](#)]
113. Miyamoto, S.; Kollman, P.A. Settle: An analytical version of the SHAKE and RATTLE algorithm for rigid water models. *J. Comput. Chem.* **1992**, *13*, 952–962. [[CrossRef](#)]
114. Laskowski, R.A.; Swindells, M.B. LigPlot+: Multiple Ligand–Protein Interaction Diagrams for Drug Discovery. *J. Chem. Inf. Model.* **2011**, *51*, 2778–2786. [[CrossRef](#)]
115. McDonald, I.K.; Thornton, J.M. Satisfying Hydrogen Bonding Potential in Proteins. *J. Mol. Biol.* **1994**, *238*, 777–793. [[CrossRef](#)]
116. Wallace, A.C.; Laskowski, R.A.; Thornton, J.M. LIGPLOT: A program to generate schematic diagrams of protein-ligand interactions. *Protein Eng.* **1995**, *8*, 127–134. [[CrossRef](#)]
117. Liu, M.; Wang, L.; Sun, X.; Zhao, X. Investigating the Impact of Asp181 Point Mutations on Interactions between PTP1B and Phosphotyrosine Substrate. *Sci. Rep.* **2014**, *4*, 5095. [[CrossRef](#)]
118. Cao, Z.; Ding, X.; Peng, B.; Zhao, Y.; Ding, J.; Watts, A.; Zhao, X. Novel expression and characterization of a light-driven proton pump archaeorhodopsin 4 in a Halobacterium salinarum strain. *Biochim. Biophys. Acta.* **2015**, *1847*, 390–398. [[CrossRef](#)]
119. Krebs, M.P.; Mollaaghbababa, R.; Khorana, H.G. Gene replacement in Halobacterium halobium and expression of bacteriorhodopsin mutants. *Proc. Natl. Acad. Sci. USA* **1993**, *90*, 1987–1991. [[CrossRef](#)]
120. Krebs, M.P.; Hauss, T.; Heyn, M.P.; RajBhandary, U.L.; Khorana, H.G. Expression of the bacteriorhodopsin gene in Halobacterium halobium using a multicopy plasmid. *Proc. Natl. Acad. Sci. USA* **1991**, *88*, 859–863. [[CrossRef](#)]
121. Cline, S.W.; Lam, W.L.; Charlebois, R.L.; Schalkwyk, L.C.; Doolittle, W.F. Transformation methods for halophilic archaeobacteria. *Can. J. Microbiol.* **1989**, *35*, 148–152. [[CrossRef](#)]
122. Ming, M.; Lu, M.; Balashov, S.P.; Ebrey, T.G.; Li, Q.; Ding, J. pH dependence of light-driven proton pumping by an archaeorhodopsin from Tibet: Comparison with bacteriorhodopsin. *Biophys. J.* **2006**, *90*, 3322–3332. [[CrossRef](#)]
123. Luecke, H.; Schobert, B.; Cartailler, J.-P.; Richter, H.-T.; Rosengarth, A.; Needleman, R.; Lanyi, J.K. Coupling photoisomerization of retinal to directional transport in bacteriorhodopsin. *J. Mol. Biol.* **2000**, *300*, 1237–1255. [[CrossRef](#)] [[PubMed](#)]
124. Lanyi, J.K.; Schobert, B. Crystallographic Structure of the Retinal and the Protein after Deprotonation of the Schiff Base: The Switch in the Bacteriorhodopsin Photocycle. *J. Mol. Biol.* **2002**, *321*, 727–737. [[CrossRef](#)]
125. Wang, T.; Sessions, A.O.; Lunde, C.S.; Rouhani, S.; Glaeser, R.M.; Duan, Y.; Facciotti, M.T. Deprotonation of D96 in Bacteriorhodopsin Opens the Proton Uptake Pathway. *Structure* **2013**, *21*, 290–297. [[CrossRef](#)] [[PubMed](#)]
126. Schobert, B.; Brown, L.S.; Lanyi, J.K. Crystallographic Structures of the M and N Intermediates of Bacteriorhodopsin: Assembly of a Hydrogen-bonded Chain of Water Molecules Between Asp-96 and the Retinal Schiff Base. *J. Mol. Biol.* **2003**, *330*, 553–570. [[CrossRef](#)]
127. Nango, E.; Royant, A.; Kubo, M.; Nakane, T.; Wickstrand, C.; Kimura, T.; Tanaka, T.; Tono, K.; Song, C.; Tanaka, R.; et al. A three-dimensional movie of structural changes in bacteriorhodopsin. *Science* **2016**, *354*, 1552–1557. [[CrossRef](#)]
128. Neutze, R.; Pebay-Peyroula, E.; Edman, K.; Royant, A.; Navarro, J.; Landau, E.M. Bacteriorhodopsin: A high-resolution structural view of vectorial proton transport. *Biochim. Biophys. Acta.* **2002**, *1565*, 144–167. [[CrossRef](#)]
129. Wickstrand, C.; Dods, R.; Royant, A.; Neutze, R. Bacteriorhodopsin: Would the real structural intermediates please stand up? *Biochim. Biophys. Acta.* **2015**, *1850*, 536–553. [[CrossRef](#)]
130. Lanyi, J.K. Proton transfers in the bacteriorhodopsin photocycle. *Biochim. Biophys. Acta.* **2006**, *1757*, 1012–1018. [[CrossRef](#)]